The Critical Role of Ligand Flexibility on the Activity of Free and Immobilized Mn Superoxide Dismutase Mimics

Micaela Richezzi, Sharon Signorella, Claudia Palopoli, Nora Pellegri, Christelle Hureau, Sandra R Signorella

inorganics

MDPI

Article

The Critical Role of Ligand Flexibility on the Activity of Free and Immobilized Mn Superoxide Dismutase Mimics

Micaela Richezzi [1], Sharon Signorella [1], Claudia Palopoli [1,*], Nora Pellegri [2], Christelle Hureau [3] and Sandra R. Signorella [1,*]

[1] IQUIR (Instituto de Química Rosario), Consejo Nacional de Investigaciones Científicas y Técnicas (CONICET), Facultad de Ciencias Bioquímicas y Farmacéuticas, Universidad Nacional de Rosario, Suipacha 531, Rosario 2000, Argentina; richezzi@iquir-conicet.gov.ar (M.R.); ssignorella@iquir-conicet.gov.ar (S.S.)

[2] IFIR (Instituto de Física Rosario), Consejo Nacional de Investigaciones Científicas y Técnicas (CONICET), Facultad de Ciencias Exactas, Ingeniería y Agrimensura, Universidad Nacional de Rosario, 27 de Febrero 210 bis, Rosario 2000, Argentina; pellegri@ifir-conicet.gov.ar

[3] LCC (Laboratoire de Chimie de Coordination) CNRS, Université de Toulouse, 205 Route de Narbonne, 31077 Toulouse, France; christelle.hureau@lcc-toulouse.fr

* Correspondence: palopoli@iquir-conicet.gov.ar (C.P.); signorella@iquir-conicet.gov.ar (S.R.S.)

Abstract: In low-molecular-weight Mn superoxide dismutase (SOD) mimics, the ligand plays a key role in tuning the reactivity of the metal center with $O_2^{\bullet-}$. We used three ligands differing in their donor sites, flexibility and/or charge, to compare the redox properties and SOD activity of the resulting Mn complexes: 1,3-bis[(pyridin-2-ylmethyl)(propargyl)amino]propane (pypapn), 1,3-bis(pyridin-2-ylmethyleneamino)propane (py_2pn) and 1,4-bis(salicylidenamino)butane (H_2salbn). These ligands afford Mn complexes that, in aqueous solution, exist as mononuclear species $[Mn(II)(pypapn)(H_2O)_2]^{2+}$, $[Mn(II)(py_2pn)(H_2O)_2]^{2+}$ and $[Mn(III)(salbn)(H_2O)_2]^{+}$. The relative reactivity of these compounds with $O_2^{\bullet-}$ at pH 7.8, $[Mn(pypapn)(H_2O)_2]^{2+}$ > $[Mn(salbn)(H_2O)_2]^{+}$ > $[Mn(py_2pn)(H_2O)_2]^{2+}$, is independent of the redox potential but strongly depends on the ligand flexibility which becomes a critical feature when the reaction occurs through an inner-sphere electron-transfer mechanism. Immobilization was used to isolate and protect the catalyst from dissociation or dimerization during catalysis. $[Mn(pypapn)(H_2O)_2]^{2+}$, with the alkyne group, was covalently grafted to azide functionalized mesoporous silica through click chemistry, while $[Mn(py_2pn)(solv)_2]^{2+}$ and $[Mn(salbn)(solv)_2]^{+}$ were encapsulated in SBA-15 mesoporous silica through ionic exchange. The retention or enhancement of the SOD activity and the improved stability of the covalently attached catalyst and the doubly charged complex encapsulated in the silica pores, make them suitable for use in aqueous media.

Keywords: Mn bioinspired catalysts; mesoporous silica; click chemistry; encapsulation; SOD activity

Citation: Richezzi, M.; Signorella, S.; Palopoli, C.; Pellegri, N.; Hureau, C.; Signorella, S.R. The Critical Role of Ligand Flexibility on the Activity of Free and Immobilized Mn Superoxide Dismutase Mimics. *Inorganics* **2023**, *11*, 359. https://doi.org/10.3390/inorganics11090359

Academic Editor: Philippe Schollhammer

Received: 8 August 2023
Revised: 27 August 2023
Accepted: 28 August 2023
Published: 30 August 2023

1. Introduction

Superoxide radical ($O_2^{\bullet-}$) is produced as a by-product of oxygen metabolism under normal physiological conditions. To prevent $O_2^{\bullet-}$ from reacting with exposed targets, large amounts of highly efficient $O_2^{\bullet-}$ scavengers are loaded in cells [1]. In healthy organisms, the intracellular $O_2^{\bullet-}$ production is balanced by its scavenger-mediated decomposition. Superoxide dismutase enzymes (SODs) are the frontline defense to remove $O_2^{\bullet-}$, catalyzing its conversion into O_2 and H_2O_2 at extremely high rates, with catalytic constant near the diffusion-controlled limit [2]. Among them, MnSOD is present in the mitochondrial matrix of eukaryotes and various prokariotes. The active site of MnSODs contains one Mn ion in a trigonal bipyramidal geometry, bound to $N_{3(his)}O_{(Asp)}$, and OH^- or H_2O, in the Mn(III) and Mn(II) forms of the enzyme, respectively [3]. In a number of pathologies such as cancer, multiple sclerosis, Alzheimer's or Parkinson's diseases, the $O_2^{\bullet-}$ overproduction exceeds the

capacity of endogenous defenses to suppress it, giving rise to oxidative stress and cell damage [4]. The limited success of the therapeutic treatment of these disorders with exogenous SODs has stimulated the search for low molecular weight catalytic scavengers of $O_2^{\bullet -}$ [5–8]. Inspired by the active site of MnSOD, a number of mononuclear Mn complexes, with different types of ligands and geometry around the metal center have been tested as MnSOD mimics [9–11]. However, in most cases these complexes are poorly soluble in aqueous solution or suffer metal dissociation and/or oligomerization during reaction [12–14]. The immobilization on mesoporous supports, either by covalent anchoring or encapsulation, has proven to be effective in protecting the catalyst, improving its stability and increasing the catalytic efficiency in terms of turnover numbers [15–19]. Among mesostructured inorganic solids, mesoporous silicas are excellent candidates for biomedical applications due to their biocompatibility, high specific surface area, controlled pores and particles size, excellent chemical and mechanical stability, and modifiable surface properties [20,21]. In this work, two N_4-tetradentate ligands, 1,3-bis[(pyridin-2-ylmethyl)(propargyl)amino]propane (pypapn) and 1,3-bis(pyridin-2-ylmethyleneamino)propane (py_2pn), and the N_2O_2-tetradentate ligand 1,4-bis(salicylidenamino)butane (H_2salbn) (Scheme 1), were chosen to evaluate the influence of the flexibility of the ligand and the nature of the donor sites (amine/pyrine, imine/pyridine, and imine/phenolate) on the redox properties and SOD activity of their Mn complexes. Besides, with the intention of lengthening the lifetime and efficiency of the catalyst, the Mn complex of pypapn, which contains the propargyl group, was covalently attached to azido functionalized mesoporous silica through "click reaction", while the Mn complexes formed with the Schiff base ligands were inserted into the channels of mesoporous SBA-15 silica by ionic exchange, and the effect of covalent grafting and encapsulation on the catalytic activity of the MnSOD mimics was assessed.

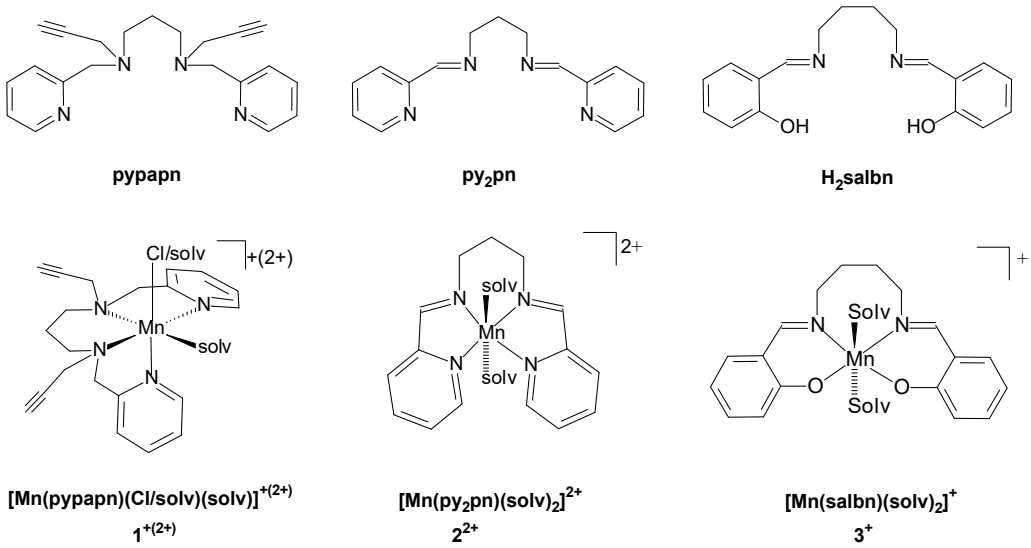

Scheme 1. Ligands and their Mn complexes in solution.

2. Materials and Methods

The reagents and the solvents used in this study were commercial products of the highest available purity and were further purified by standard methods, as necessary.

2.1. Synthesis of Ligands, Complexes and Hybrid Materials

N,N′-bis(2-pyridylmethylen)propane-1,3-diamine (py_2pn) [22], and N,N′-bis(salicylidene)butane-1,4-diamine (H_2salbn) [23], were prepared according to literature procedures.

2.1.1. Synthesis of 1,3-Bis[(2-Pyridilmethyl)(Propargyl)Amino]Propane (Pypapn)

The synthesis of pypapn was adapted from the previously reported procedure for a similar ligand [19]. An excess of sodium borohydride was added to a methanolic solution

(16 mL) of N,N′-bis(2-pyridinylmethylen)propane-1,3-diamine (0.425 g, 1.7 mmol), and the mixture was stirred for 2 h at room temperature. Afterwards, the solvent was evaporated, and the product was redissolved in a water/methanol (35:65, 20 mL) mixture. Three extractions with dichloromethane (3 × 12 mL) were performed. The organic phases were washed with water (12 mL) and dried over anhydrous sodium sulphate. The mixture was filtered, the solvent was evaporated and the solid was dissolved in THF (8 mL). After the addition of potassium carbonate (0.892 g, 6.4 mmol), propargyl bromide (0.350 mL, 3.34 mmol) was added dropwise to the stirred mixture. The reaction was left for 20 h at 50 °C. Then, the solvent was evaporated, and the product dissolved in dichloromethane before performing a filtration through a potassium carbonate pad. A light brown oil was obtained after evaporation of the dichloromethane. Yield: 0.458 g (1.38 mmol, 81%). ESI-MS (methanol): m/z = 333.2 $[C_{21}H_{24}N_4 + H]^+$. ^{1}H NMR ($CDCl_3$, δ, ppm): 8.55 (dt, 2H, H2, J = 1; 5 Hz), 7.62 (td, 2H, H4, J = 1.9; 7.9 Hz), 7.39 (d, 2H, H5, J = 7.9 Hz), 7.14 (ddd, 2H, H3, J = 1; 5; 7.9 Hz), 3.79 (s, 2H, H6), 3.39 (d, 4H, H7, J = 2.4 Hz), 2.64 (q, 4H, H10, J = 7.4 Hz), 2.21 (t, 2H, H9, J = 2.4 Hz), 1.73 (qint, 2H, H11, J = 7.4 Hz). ^{13}C NMR ($CDCl_3$, δ, ppm): 158.09 (C1), 148.23 (C2), 135.42 (C4), 122.06 (C5), 121.00 (C3), 77.38 (C8), 72.21 (C9), 58.71 (C6), 50.43 (C10), 41.05 (C7), 24.49 (C11). Significant IR bands (NaCl, ν, cm^{-1}): 3300, 2945, 2832, 2099, 1591, 1571, 1475, 1433, 760 (Figures S1 and S2a).

2.1.2. Synthesis of [Mn(Pypapn)Cl]Cl·0.5 H_2O (**1**)

A solution of $MnCl_2$ tetrahydrate (0.119 g, 0.60 mmol) in methanol (1 mL) was slowly added to a solution of ligand pypapn (0.210 g, 0.63 mmol) in methanol (1 mL). The reaction mixture was stirred at room temperature for 4 h. Then, hexane was added, and the mixture was left overnight at 4 °C. The light beige solid was filtered, washed with cold methanol, dichloromethane and hexane, and dried under vacuum. Yield: 0.156 g (0.34 mmol, 57%). Anal. calcd. for $C_{21}Cl_2H_{24}MnN_4{\cdot}0.5H_2O$: C 54.0, H 5.40, N 12.0%. Found: C 54.3, H 5.5, N 11.9%. UV-vis, λ_{max} nm (ε M^{-1} cm^{-1}) in methanol: 261 (13,200). Significant IR bands (KBr, ν, cm^{-1}): 3429, 3228, 3058, 2958, 2937, 2872, 2105, 1608, 1574, 1479, 1449, 1094, 1019, 782, 707, 641. ESI-MS (methanol): m/z = 440.1 $[Mn(pypapn)(H_2O)Cl]^+$. Conductivity: 145 Ω^{-1} cm^2 mol^{-1} in methanol.

2.1.3. Synthesis of $[Mn_2(Py_2pn)_3(ClO_4)_2](ClO_4)_2{\cdot}2H_2O$ (**2**)

A deoxygenated solution of $Mn(ClO_4)_2$ hexahydrate (0.215 g, 0.60 mmol) in ethanol (2 mL) was added to a previously deoxygenated solution of ligand py_2pn (0.152 g, 0.60 mmol) in dichloromethane (2 mL). The reaction mixture was stirred at room temperature, under an N_2 atmosphere and light-protected for 6 h. The yellow precipitate was filtered, washed with ethanol, dichloromethane and hexane, and dried under vacuum. Yield: 0.130 g (0.1 mmol, 33%). Anal. calcd. for $C_{45}Cl_4H_{48}Mn_2N_4O_{16}{\cdot}2H_2O$: C 41.6, H 4.03, N 12.9, Mn 8.4%. Found: C 41.2, H 3.94, N 12.8, Mn 8.2%. UV-vis, λ_{max} nm (ε M^{-1} cm^{-1}) in MeCN: 280 (4660). Significant IR bands (KBr, ν, cm^{-1}): 3423, 3062, 2929, 2853, 1645, 1596, 1569, 1478, 1440, 1145, 1119, 1083, 782, 637, 626. ESI-MS (DMF): m/z = 406 $[Mn(py_2pn)(ClO_4)]^+$, 153.5 $[Mn(py_2pn)]^{2+}$. Conductivity: 246 Ω^{-1} cm^2 mol^{-1}, in MeCN:MeOH 3:7.

2.1.4. Synthesis of $[Mn_2(Salbn)_2OH]ClO_4$ (**3**)

An aqueous solution of NaOH (0.450 mL, 5.13 M) was added to a solution of ligand H_2salbn (0.68 g, 2.4 mmol) in a methanol/ethanol mixture (1:1, 18 mL). Subsequently, a solution of Mn(II) perchlorate hexahydrate was added dropwise (0.892 g, 2.4 mmol) in the same solvent mixture (3.0 mL). The reaction mixture was stirred for 2 h at reflux temperature and overnight at room temperature. The green solid was collected by filtration, washed with cold methanol and hexane, and dried under vacuum. Yield: 0.741 g (0.91 mmol, 76%). Anal. calcd. for $C_{36}ClH_{37}Mn_2N_4O_9$: C 53.1, H 4.6, N 6.9, Mn 13.5%. Found: C 53.6, H 4.9, N 7.0, Mn 13.0%. UV-Vis, λ_{max} nm (ε, M^{-1} cm^{-1}) in MeOH: 277 (11,560), 306 (8218), 393 (3760), 610 (196); in CH_3CN: 279 (15,914), 302 (11,190), 382 (4695), 614 (308). Significant IR bands (KBr, ν, cm^{-1}): 3452, 3063, 2936, 2874, 1650, 1608,1288, 1093, 774, 623. Conductivity:

98.6 Ω^{-1} cm^2 mol^{-1}, in DMF. The addition of 4.8 mmol of NaOH maintaining constant all the other conditions, yielded [Mn(salbn)O]$_2$ (**4**), as a brown solid. Anal. calcd. for $C_{36}H_{36}Mn_2N_4O_4$: C 59.2, H 5.0, N 7.7%. Found: C 58.8, H 5.1, N 7.5%.

Caution! *The perchlorate salts used in this study are potentially explosive and should be handled with care.*

2.1.5. Synthesis of "Click" Modified Silica Pypntriazole@OP-MS

The azidopropyl functionalized silica, N_3pn@OP-MS, was prepared by co-condensation of TEOS (tetraethylorthosilicate) and AzPTES (3-azidopropyltriethoxysilane), with Pluronic P-123 as a structure-directing agent, following a recently reported procedure [19]. The obtained material (300 mg) was suspended in a methanol/acetonitrile mixture (75:25, 72 mL) and stirred for 10 minutes. Afterwards, a solution of the ligand pypapn (30 mg, 0.09 mmol) in the same solvent mixture (9 mL) was added. The reaction mixture was stirred for 1 h, and then the solid catalyst CuBr(PPh$_3$)$_3$ (84 mg, 0.09 mmol) was added. The mixture was left to stir at 60 °C until the complete disappearance of the azide stretching band at 2114 cm^{-1} in the IR spectrum. The product was filtered, washed using Soxhlet extraction with dichloromethane, and the solid was dried at 60 °C. A solution of $MnCl_2 \cdot 4H_2O$ (32 mg, 0.16 mmol) in methanol (1 mL) was added to a suspension of the obtained material (50 mg) in methanol (5 mL). The mixture was stirred for a week at room temperature. The product was filtered, washed with methanol and dichloromethane, and dried at 60 °C, to afford 45 mg of Mn-pypntriazole@OP-MS. Anal. (wt.%): N 1.3, Mn 0.7. Catalyst' content: 13 mmol/100g. Significant IR bands (KBr, ν cm^{-1}): 1640 (δ, H-O-H), 1080 (ν_{as}, Si-O), 795 (ν_s, Si-O), 463 (δ, Si-O-Si).

2.1.6. Encapsulation of Complexes **2** and **3** in Mesoporous Silica SBA-15

Mesoporous silica SBA-15 was synthesized as previously reported [24]. Compound **2** (83 mg, 0.07 mmol) was dissolved in a mixture of acetonitrile/methanol (1:2, 7 mL) and slowly added to silica SBA-15 (60 mg). The mixture was stirred at room temperature for 24 h and filtered. Then, the solid was suspended in methanol (1 mL) and stirred for 5 h. The resulting material was filtered and washed with methanol and dichloromethane and dried at 60 °C for 48 h, yielding 55 mg of **2**@SBA-15. Anal. (wt.%): N 0.85, Mn 0.8. Catalyst content: 15 mmol/100 g. Following the same procedure, 140 mg of **3**@SBA-15 were obtained, with a catalyst content of 4 mmol/100 g. Significant IR bands (KBr, ν cm^{-1}): 1640 (δ, H-O-H), 1080 (ν_{as}, Si-O), 795 (ν_s, Si-O), 463 (δ, Si-O-Si).

2.2. Analytical and Physical Measurements

2.2.1. Analytical Measurements

Metal content was determined with an Inductively coupled plasma mass spectrometer (ICP-MS) Perkin Elmer NexION 350× (PerkinElmer, Waltham, MA, USA). CHN analyses were performed on a PERKIN ELMER 2400 series II Analyzer.

2.2.2. Spectroscopy Measurements

Infrared spectra were recorded in the 4000–400 cm^{-1} range on a Perkin-Elmer Spectrum One FTIR spectrophotometer provided with a DTGS detector, resolution = 4 cm^{-1} and 10 accumulations. FT-IR spectra were registered from KBr sample pellets. UV–visible spectra were recorded on a Jasco V-550 spectrophotometer (Jasco, Tokyo, Japan). Electron Paramagnetic Resonance (EPR) spectra were obtained at 115 K on an Elexsys E 500 Bruker spectrometer (Bruker, Billerica, MA, USA), operating at a microwave frequency of approximately 9.5 GHz and on a Bruker EMX-Plus spectrometer for measurements at Q-band. Electrospray ionization (ESI) mass spectra were obtained with a Thermo Scientific LCQ Fleet (Thermo Scientific, Waltham, MA, USA). The solutions for electrospray were prepared from solutions of complex diluted with methanol to a final ~10^{-5} M concentration. ^{1}H NMR spectra were recorded on a Bruker AC 300 NMR spectrometer at ambient probe temperature (ca. 25 °C). Chemical shifts (in ppm) are referenced to tetramethylsilane and

paramagnetic NMR spectra were acquired employing a superWEFT sequence, with an acquisition time of 80 ms.

2.2.3. Conductivity and Electrochemical Measurements

Conductivity measurements were performed on 1.0 mM solutions of the complexes using a Horiba F-54 BW conductivity meter (Horiba, Kyoto, Japan). The electrochemical experiments were performed with a Princeton Applied Research potentiostat (AMETEK, Berwyn, PA, USA), VERSASTAT II model, with the 270/250 Research Electrochemistry Software. Studies were carried out under Ar, in N,N-dimethylformamide, acetonitrile or methanol solution using 0.1 M Bu_4NBF_4 as a supporting electrolyte and $\approx 10^{-3}$ M of the complex. The working electrode was a glassy carbon disk, and the reference electrode was a calomel electrode isolated in a fritted bridge with a Pt wire as the auxiliary electrode. Under these conditions, E(ferrocene/ferrocenium) = 474 mV in DMF; 409 mV in MeOH; 388 mV in MeCN, at room temperature.

2.2.4. Electron Microscopy Measurements

The size and morphology of the solid materials were analyzed using an AMR 1000 Leitz scanning electron microscope (SEM) (Leitz, Stuttgart, Germany) operated at variable accelerating voltages and with EDX detector NORAN System SIX NSS-200 (Thermo Scientific, Waltham, MA, USA). Samples for SEM observation were prepared by dispersing a small amount of powder of dry silica and hybrid samples on double-sided conductive adhesive tabs on top of the SEM sample holders. Then, the samples were covered by a thin layer of gold deposited by sputtering to avoid charge accumulation on the surfaces. The selected accelerating voltage used in the showed images were 20 kV at high vacuum condition. Transmission electron microscopy (TEM) analysis was performed with a TEM/STEM JEM 2100 Plus with an operational voltage of 200 kV (variable), with a LaB6 filament. SEM and TEM images were processed using the public domain ImageJ program.

2.2.5. N_2 Adsorption-Desorption Measurements

N_2 adsorption-desorption isotherms were obtained at 77 K on a Micrometric ASAP 2020 V4.02 (V4.02 G) apparatus (Micrometric, Lincoln, UK). The samples were degassed at 10^{-3} Torr and 200 °C for 6 h prior to the adsorption experiment. Surface area (S_{BET}) was calculated using the Brunauer-Emmett-Teller (BET) [25] equation over the pressure range (p/p°) of 0.05–0.20. The volume of micropores and mesopores ($V_{\mu P}$ and V_{MP}) was determined by the alpha-plot method using the standard Licrospher isotherm. The total pore volume (V_{TP}) was determined with the Gurvich rule [25] at 0.98 p/p°. The pore size distributions were calculated using the Villarroel–Bezerra–Sapag (VBS) model [26], on the desorption branch of the N_2 isotherms.

2.3. Indirect SOD Assay

The SOD activity of the free and immobilized complex was tested by an indirect method measuring the inhibition of the photoreduction of nitro blue tetrazolium (NBT) [27]. The reaction mixture was prepared in phosphate buffer (pH 7.8), containing riboflavin (3.35 μM), methionine (9.52 mM), NBT (38.2 μM) and the complex either free (diluted aliquots (50 μL) of the complex solution in DMF were added to the reaction mixture) or immobilized, in different concentrations (final volume = 3.2 mL). Riboflavin was the last added and the reaction was initiated by illumination of the mixtures with a 16 W led lamp placed at 30 cm, at 25 °C. The reduction of NBT was measured at 560 nm after an illumination period of 15 min. The IC_{50} values were determined from concentration-dependent plots. Control reactions confirmed that the compounds did not react directly with NBT or riboflavin. The inhibition percentage was calculated according to:

$$IC = \frac{\left[(\Delta Abs/t)_{without\ catalyst} - (\Delta Abs/t)_{with\ catalyst}\right] \times 100}{(\Delta Abs/t)_{without\ catalyst}} \quad (1)$$

The IC_{50} values were used to calculate the McCord-Fridovich second-order rate constant (k_{McF}) [28]. On the basis of competition with NBT, at 50% inhibition, the rates of the reactions of $O_2^{\bullet -}$ with NBT and the mimic are equal, k_{McF} [complex] = k_{NBT} [NBT], where k_{NBT} (pH = 7.8) = 5.94 × 10^4 M^{-1} s^{-1}.

2.4. Preparation of Potassium Superoxide Solutions

For EPR measurements, stock KO_2 solution in anhydrous dimethylsulfoxide (DMSO) was prepared by mixing 9.3 mg of KO_2 in DMSO (5 mL) and sonicated for 15 min, followed by centrifugation at 6000 rpm for 25 min. The concentration of KO_2 in the supernatant was estimated by using its extinction coefficient 2686 M^{-1} cm^{-1} in deoxygenated DMSO solution [29] and confirmed by the horseradish peroxidase assay.

3. Results and Discussion

3.1. Characterization of Complexes

The reaction between pypapn and $MnCl_2$ in methanol leads to the formation of an Mn(II) complex, [Mn(pypapn)Cl]Cl·0.5 H_2O (**1**), that precipitates from the reaction mixture as a light beige solid after addition of hexane, at 4 °C. The FT-IR spectrum (Figure S2a) evidences the fingerprint pattern of pypapn displaying two absorption bands characteristic of the alkyne group: an intense band at 3227 cm^{-1}, corresponding to the C-H stretching of the terminal alkyne, and a weaker band at 2105 cm^{-1}, attributed to the C≡C stretching, besides the strong bands of the pyridine ring shifted by ≈10 cm^{-1} from those in the free ligand due to metal coordination, and a broad band at 3420 cm^{-1} due to the presence of water. In addition, the ring breathing band observed at 998 cm^{-1} in the free ligand, is replaced by two new bands at 1033 and 1017 cm^{-1}, reinforcing the coordination of pyridine to Mn(II). The X-band EPR spectrum recorded on the powdered complex shows broad absorptions on the full magnetic field, far from $g_{eff} \approx 2$ (Figure 1a,b). At 120 K the main transition is observed at g_{eff} = 2.9 flanked by two minor ones at g_{eff} = 5.7 and 1.5, with little effect of temperature variation from 120 K to 291 K on the main spectral features except for an additional minor line observed at g_{eff} = 14 at 291 K. A similar EPR spectrum was obtained for the diluted DMSO frozen solution of the complex (Figure 1c), suggesting the large linewidth is not the result of spin-spin intermolecular interactions. However, in this spectrum, an additional signal is observed at g_{eff} = 2.02, which might correspond to the complex formed by the substitution of bound chloride by a solvent molecule, in agreement with conductivity results (see below).

The fine structure pattern of the EPR spectra of powdered **1** is characteristic of low symmetry Mn(II) complexes where the magnitude of the zero field splitting (*zfs*) of the spin states of the high spin d^5 metal ion compete with the Zeeman interaction [30–34]. For high-spin Mn(II) complexes, the shape of the EPR spectra mainly depends on the *zfs* terms since the anisotropy of the Zeeman interaction is very small and leads to g values close to 2. In particular, for chloro-Mn(II) complexes, *zfs* is mostly governed by the anionic halide ligand with the major contribution originating from the interference between metal and halide spin-orbit coupling, while is less sensitive to the coordination number or the nature of the other ligands [33,35]. Nevertheless, the analysis of the X-band EPR spectra is difficult because of the mixture between the Zeeman levels.

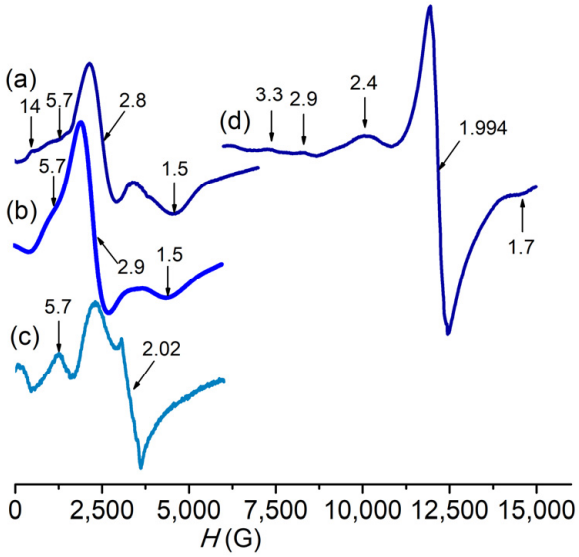

Figure 1. X-band EPR spectra of **1** (**a**) powder at 291 K (ν = 9.88 MHz), (**b**) powder at 120 K (ν = 9.31 MHz), (**c**) frozen DMSO solution at 120 K (ν = 9.31 MHz), and (**d**) Q-band EPR spectrum of powdered **1** at 291 K (ν = 33.97 MHz).

In the Q-band EPR spectrum of powdered **1** recorded at room temperature (Figure 1d), the magnitude of the *zfs* is smaller than the energy of the microwave provided by the spectrometer, transitions are better resolved, and an estimation of the *D* and *E* values (the axial and rhombic *zfs* parameters, respectively) could be done [36]. At room temperature, the features present in the Q-band EPR spectrum around g_{eff} = 2, associated with the $|5/2, -1/2> \rightarrow |5/2, +1/2>$ transitions along the x, y and z magnetic axes, become prominent to the detriment of the side signals corresponding to transitions between $\pm 5/2$ and $\pm 3/2$, and $\pm 3/2$ and $\pm 1/2$ Zeeman levels. D = 0.11 cm^{-1} and rhombicity E/D = 0.29 values were estimated for **1** as described elsewhere [36], which are in the range of other chloro-Mn(II) complexes [33,37–39]. The retention of bound chloride in solution is inferred by the similar EPR spectra in the solid and in frozen solution, except for the signal at g = 2, probably due to a minor amount of solvated Mn(II) complex formed through ligand exchange, only observed in the frozen DMSO solution. The variations between the two signatures (in the solid versus frozen solution) are attributed to a slightly different structure in the solution due to the release of solid-state constraints. Therefore, the fine structure in the EPR spectra must be due to a distorted mononuclear chloro-Mn(II) species in the solid state as well as in solution, as confirmed by ESI-MS measurements (see below).

Precipitation of AgCl after the addition of $AgNO_3$ to a solution of the complex in methanol corroborates the presence of chloride anion as counterion. The molar conductivity of the complex in methanol is 145 Ω^{-1} cm^2 mol^{-1}, a value somewhat higher than expected for a 1:1 electrolyte [40], suggesting slight ligand exchange occurs upon dissolution of the complex affording a mixture of $[Mn(pypapn)Cl(solvent)]^+$ ($\mathbf{1}^+$) and a minor proportion of $[Mn(pypapn)(solvent)_2]^{2+}$ ($\mathbf{1}^{2+}$), as already observed for other chloro-Mn(II) complexes [41]. The positive mode ESI-mass spectrum of the complex in methanol confirms its chemical composition in solution, with the parent peak at m/z = 440.1 (100%) and a minor one at m/z = 454.1 (8%), which originate from the monocations $[Mn(pypapn)Cl(H_2O)]^+$ and $[Mn(pypapn)Cl(CH_3OH)]^+$, respectively (Figure 2a). The isotopic pattern of these peaks matches the simulated spectra well. Two other intense peaks originating from ligand fragmentation and exchange are observed at m/z 395.1 (95%) and 430.1 (90%), whose mass and isotope distribution patterns correspond to $[Mn(pypapn—C_2H_3)Cl]^+$ and $[Mn(pypapn—C_2H_3)Cl_2]^+$, respectively. Besides, no dimeric species are observed in the mass spectra of freshly prepared solutions of the complex in any solvent.

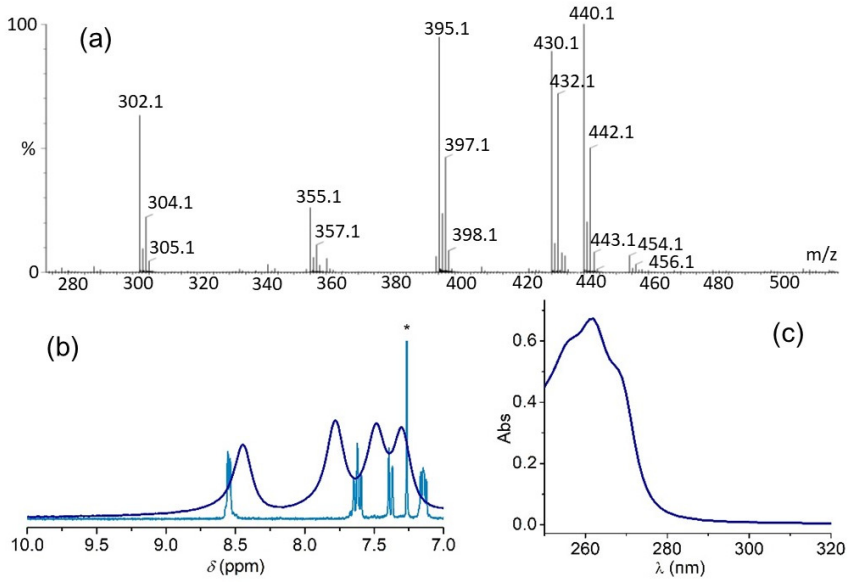

Figure 2. (**a**) ESI-mass spectrum of 1 in methanol. (**b**) 10–7 ppm region of the ^{1}H NMR spectra of **1** in D_4-methanol (blue line) and pypapn in Cl_3CD (light blue line). *: solvent. (**c**) UV-vis spectrum of 5×10^{-5} M **1** in MeOH.

Further evidence of the coordination of the ligand to Mn(II) is provided by the ^{1}H NMR spectrum of the complex (Figure S2b) that shows the broadening of the resonances of the pyridine ring protons as well as those from the methylene groups bound to the amino-*N*, with halfwidths of 100 to 200 Hz, as a result of the paramagnetic relaxation induced by Mn(II) [42,43]. In addition, the signals of the pyridine ring protons shift between 0.1 and 0.2 ppm compared to the free ligand (shown in Figure 2b), while the methylene protons undergo broadening but keep their original chemical shift (Figure S2b). Three strong intraligand $\pi \rightarrow \pi^*$ transitions at 256, 261 and 267 nm prevail in the electronic spectrum of **1** in methanol (Figure 2c) and prevent observation of the charge transfer band. For the diluted complex solutions (<1×10^{-4} M) employed in this work, the electronic spectrum is featureless at wavelengths longer than 300 nm, as expected for a Mn(II) complex.

Complex **2,** was obtained as a light yellow solid after a reaction of equimolar amounts of py_2pn and $Mn(ClO_4)_2$, in a 1:1 EtOH:Cl_2CH_2 mixture, at room temperature and anaerobic conditions. From elemental analysis, the obtained solid can be formulated as $[Mn_2(py_2pn)_3(ClO_4)_2](ClO_4)_2$. A comparison of FT-IR spectra of py_2pn and the complex (Figure S3a) provides some clues on the ligand binding in **2**. The C=N stretching band at 1648 cm^{-1} in the ligand shifts to 1645 cm^{-1} in **2** as a result of metal coordination to the imino-*N*. The pyridine ring stretching vibrations of the ligand at 1588, 1567, 1469 and 1437 cm^{-1} shift to 1596, 1569, 1478 and 1440 cm^{-1} and undergo variations in their relative intensities. The last has been observed when different pyridine groups bind Mn with distinct strength [22]. Additionally, the strong bands observed in the ranges of 1145–1074 cm^{-1} and 637–626 cm^{-1} evidence the presence of bound and free perchlorate. The ligand to metal stoichiometric ratio in the solid suggests one of the ligands might bridge the two Mn(II) ions like in the diMn(II) complex, $[Mn_2(py_2en)_3(ClO_4)_2](ClO_4)_2$, obtained with the corresponding Schiff-base ligand having an ethylene bridge (py_2en = N,N′-bis(2-pyridylmethylen)ethane-1,2-diamine) [22]. In $[Mn_2(py_2en)_3(ClO_4)_2](ClO_4)_2$, each one of the two terminal py_2en ligands is bound to one Mn(II) ion, two of the perchlorate ions are coordinated to the two metal ions as capping ligands, while the third py_2en acts as compartmental binucleating ligand with each Mn(II) ion bound to one of the N_{im},N_{py} donor sets. Curiously, in that previous work, the reaction of py_2pn and $Mn(ClO_4)_2$, afforded the mononuclear complex, $[Mn(py_2pn)(H_2O)_2](ClO_4)_2$, in the same solvent mixture as the one used in the present work, but in aerobic conditions. Conductivity and ESI-MS studies reveal that upon dissolution the compartmental bridging py_2pn dissociates and **2** converts into the mononuclear $[Mn(py_2pn)]^{2+}$ ($\mathbf{2}^{2+}$) complex.

The molar conductivity of the complex in acetonitrile/MeOH is 246 Ω^{-1} cm^2 mol^{-1}, a value expected for a 1:2 electrolyte in this solvent mixture [40]. ESI-mass spectra registered in either protic or aprotic solvents confirm the presence of mononuclear species in the solution. In DMF, the positive mode ESI-mass spectrum registered with a cone voltage of 30 V, (Figure 3a) exhibits one peak at m/z 153.5 (80%), whose mass and isotopic distribution pattern correspond to the $[Mn(py_2pn)]^{2+}$ dipositive cation. Two other minor peaks belonging to complex monocations are observed at m/z 307.1 (10%) and 406.0 (35%), and can be assigned to $[Mn(py_2pn)]^{+}$ and $[Mn(py_2pn)(ClO_4)]^{+}$, respectively. The $[Mn(py_2pn)(CHO_2)]^{+}$ adduct, generated with formate present in the spectrometer, is also observed at m/z 352.1 (70%).

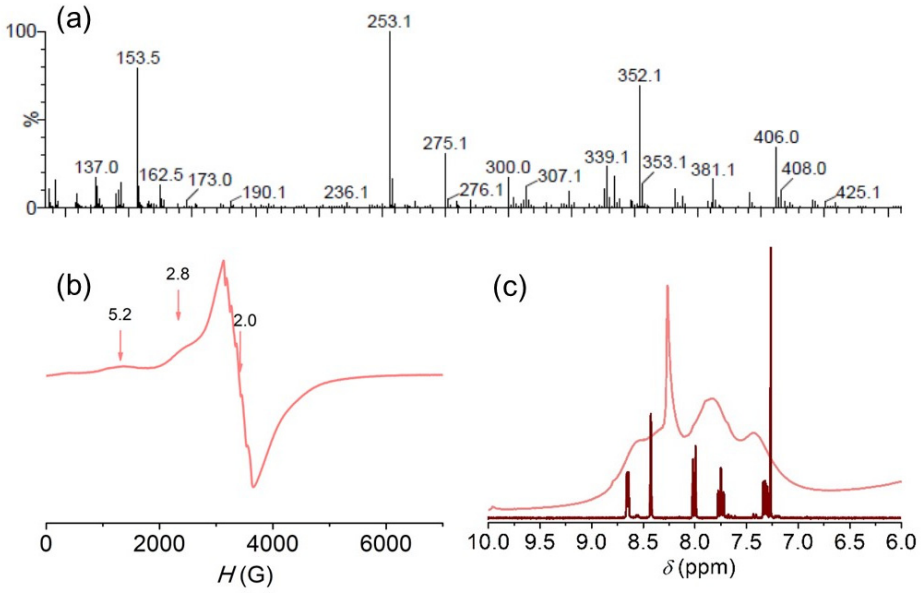

Figure 3. (**a**) Positive ESI-mass spectrum of **2** in DMF. Voltage cone = 30 V. (**b**) X-band EPR spectrum of **2** in DMSO. T = 120 K. (**c**) ^{1}H NMR spectra of py_2pn in Cl_3CD (brown line) and **2** in D_6-DMSO (orange line).

When a cone voltage of 50 V is used, the major peak (m/z = 307.1, 100%) corresponds to $[Mn(py_2pn)]^{+}$, while $[Mn(py_2pn)]^{2+}$ is much less abundant or not observed (Figure S3c). Therefore, the relative proportion of $[Mn(py_2pn)]^{+}$ and $[Mn(py_2pn)]^{2+}$ species in the spectra depends on the cone voltage employed in the ESI-MS measurements [44], suggesting $[Mn(py_2pn)]^{+}$ should be generated by the reduction of the parent $[Mn(py_2pn)]^{2+}$ in the spectrometer. The negative mode ESI-mass spectrum is dominated by the peaks at m/z = 98.95 and 100.95 (M + 2) of the perchlorate anion. The presence of free ligand (Hpy_2pn^{+}: m/z = 253.1, 100%) in the spectra reinforces the proposed structure for the solid compound, since the formation of $[Mn(py_2pn)]^{2+}$ ($\mathbf{2}^{2+}$) upon dissolution of **2**, implies the release of free ligand to the solution.

Although the synthesis of the complex was carried out in an inert atmosphere, **2** is stable towards oxidation as evidenced by the electronic spectrum of the complex in acetonitrile (Figure S3b) that only shows a strong band at 280 nm and a shoulder at 292 nm assigned to intraligand π-π^* transitions overlapped to charge transfer transitions without noticeable electronic transitions at longer wavelengths. UV-vis spectra registered at different times after preparing the solution (up to 24 h), showed identical molar absorption coefficients, indicating that the complex is stable in solution. In this sense, the X-band EPR spectrum of a frozen DMSO solution of **2** shows a six-line signal centered at g = 2, with hyperfine splitting of 89 $\times$ 10^{-4} cm^{-1}, characteristic of a mononuclear Mn(II) complex (Figure 3b). The two additional signals observed at g_{eff} = 5.2 and g_{eff} = 2.8 are typical of Mn(II) with zero fields splitting slightly weaker than the X-band microwave frequency. The paramagnetic ^{1}H NMR spectrum of **2** in D_6-DMSO shows the line broadening of pyridine

and azomethine protons resonances that appear shifted ≈ 0.3 ppm compared to the free ligand (Figure 3c), confirming the Mn(II) coordination to these donor sites [43,45–47]. The ^{1}H NMR spectral pattern of the complex in the 10–6 ppm region, shown in Figure 3c, comprises a set of four resonances at 8.5, 8.3, 7.9 and 7.4 ppm (linewidth in the range of 150 to 200 Hz) assigned to pyridine ring protons, and one relative sharp resonance at 8.2 ppm ($w_{1/2}$ = 50 Hz) attributed to the imine proton. The methylene protons should lie in the region of 5–2 ppm obscured by the intense solvent signal (not shown). It must be noted that the signals of protons of the free ligand present in solution should be broadened by the Mn(II) paramagnetism and also contribute to the observed spectrum.

The Mn(III) complex **3** was obtained as a green solid by a reaction of $Mn(ClO_4)_2$, H_2salbn and NaOH in a 1:1:1 mole ratio, in a methanol/ethanol mixture. From elemental analysis, the solid can be formulated as $Mn_2(salbn)_2(OH)ClO_4$. The strong band at 774 cm^{-1} (Figure S4) together with the absorption at 3420 cm^{-1} in the FT-IR spectrum of this complex, suggest hydroxide may bridge the two Mn(III) ions [48,49]. The formation of the μ-OH bridged dimer in a mildly basic medium has precedent in previous reports for related Mn(III) complexes under similar conditions [50,51]. In line with this, the absorption band at 1648 cm^{-1}, corresponding to the azomethine stretching vibration, is shifted to wavenumbers higher than in the free ligand, as also observed for other hydroxo-bridged diMn(III) complex [52]. Besides, the intense absorption bands at 1095 and 625 cm^{-1}, confirm the presence of perchlorate as counterion. When the reaction was carried out employing $Mn(ClO_4)_2$, H_2salbn and NaOH in 1:1:2 mole ratio, [(salbn)Mn(IV)(μ-O)]$_2$ (**4**) was obtained as a brown solid, the FT-IR spectrum of which exhibits the characteristic four intense Mn-O stretching bands at 650, 631, 619, 603 cm^{-1} of the Mn(IV)(μ-O)$_2$Mn(IV) core [53], well different from those of **3**. Upon dissolution of **3** in a protic solvent, protonation of the hydroxide occurs and mononuclear [Mn(salbn)]$^+$ (**3**$^+$) forms, as verified by its ^{1}H NMR spectrum in D_4-methanol (Figure 4a). The paramagnetic ^{1}H NMR spectrum of the complex reveals a simple pattern of three resonances outside the diamagnetic 0–10 ppm region. One broad resonance at 12 ppm attributed to the central –$(CH_2)_2$– protons of the aliphatic chain, and two up-field paramagnetically shifted resonances at −25 and −26 ppm, which can be assigned to H5 and H4 aromatic ring protons on the basis of comparison with reported spectra for related Mn(III) complexes [54,55]. By contrast, antiferromagnetically coupled diMn(III) species show sharper signals within or closer to the diamagnetic region [51], absent in the paramagnetic ^{1}H NMR spectrum of **3**$^+$. Because of their closeness to the Mn center, protons adjacent to the donor groups of the Schiff base ligand (aromatic H3 and H6, N=CH- and CH_2-N=C) are not observed in the explored spectral window (200 to −200 ppm) [56]. The equivalence of protons of the two aromatic rings indicates that the tetradentate Schiff base ligand is symmetrically arranged around the Mn(III) ion [54,57,58].

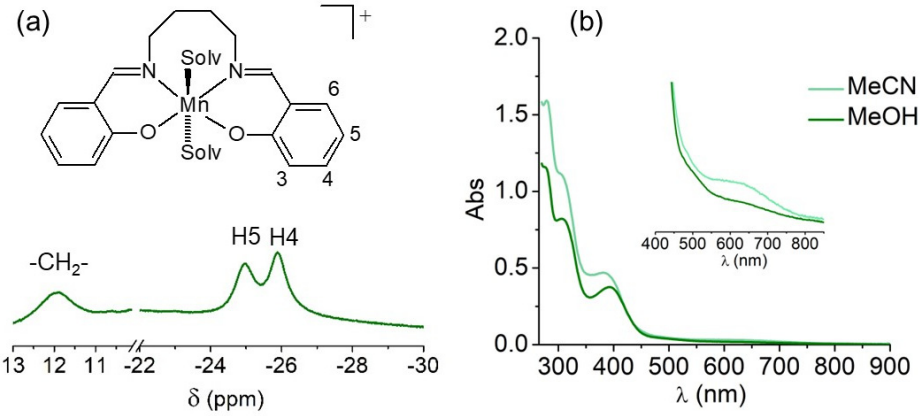

Figure 4. (**a**) ^{1}H NMR spectrum of **3**$^+$ in D_4-methanol. (**b**) Electronic spectra of 1 × 10^{-4} M **3**$^+$ in acetonitrile and methanol. Inset: View of the d-d transitions region.

The electronic spectrum of the complex in either methanol or acetonitrile shows two bands at 308 and 393 nm (Figure 4b), assigned to intraligand π-π* and n-π* transitions, respectively, the last overlapping the phenolate-to-manganese charge transfer band, and a much less intense broad band centered at 610 nm (ε = 196 M^{-1} cm^{-1}) corresponding to the d-d transition of Mn(III). The compound behaves as a 1:1 electrolyte in solution, with a molar conductivity of 98.6 Ω^{-1} cm^2 mol^{-1}, in DMF. The solution behavior of compound **3** distinguishes from **4** which behaves as a non-electrolyte in solution, exhibits an intense ligand-to-metal charge transfer at 495 nm (ε = 7200 M^{-1} cm^{-1}, Cl_2CH_2) in the electronic spectrum, is slightly soluble in methanol and is reduced at −0.46 V vs. SCE in DMSO through a two-electron process, in agreement with previously reported data for this oxidized Mn(IV) dimer [59].

3.2. Electrochemical Studies

From the previous discussion, the three complexes exist in solution as mononuclear species, $[Mn(pypapn)Cl(solv)]^+$, $[Mn(py_2pn)(solv)_2]^{2+}$ and $[Mn(salbn)(solv)_2]^+$. In these compounds, the ligand modulates the redox potential of Mn and the geometry around the metal center, two essential factors to control their reactivity with superoxide. Cyclic voltammetry was used to investigate the electrochemical properties of the three complexes (Figure 5).

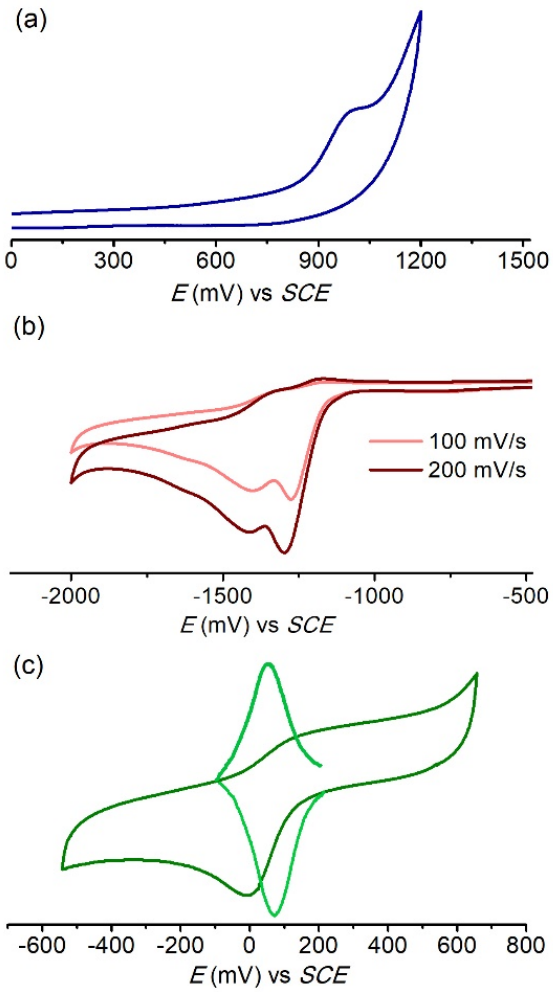

Figure 5. Cyclic voltammograms of (**a**) **1** in methanol, scan rate 100 mV/s. (**b**) **2** in DMF. (**c**) **3** in methanol, scan rate: 50 mV/s; square wave voltammogram, scan frequency: 2 Hz. Conditions: supporting electrolyte: $TBAPF_6$, working electrode: glassy carbon. [complex] = 1 mM.

In methanol, complex **1** displays an irreversible anodic wave at E_{pa} = 1.01 V vs. *SCE* attributed to the oxidation of Mn(II) to Mn(III) (Figure 5a). This wave does not correspond to the oxidation of the ligand or free chloride, which takes place at a higher potential. The lack of reversibility of the oxidation process, even at higher scan rates, is probably due to solvation and loss of bound chloride in the oxidized complex. It is known that the value of the redox potential of the Mn(II)/Mn(III) couple of chloro-Mn(II) complexes with polyamino/pyridine ligands is 0.3–0.5 V less positive than the solvato-Mn(II) complex formed by ligand exchange of chloride and a solvent molecule [32,60–62]. The observation of a decrease in the intensity of the anodic wave at 1.01 V after the addition of excess $AgNO_3$ to the complex solution suggests this wave corresponds to the oxidation of $[Mn(II)(pypapn)Cl(solv)]^+$ to $[Mn(III)(pypapn)Cl(solv)]^{2+}$, while the oxidation of the solvated complex is outside the scanned potential window. A similar anodic wave observed at E_{pa} = 1.1 V vs. *SCE* has been attributed to the irreversible oxidation of the complex $[Mn(II)LCl(OH_2)]^+$ (L = N,N′-dimethyl-N,N′-bis(2-pyridilmethyl)propane-1,3-diamine), bearing a methyl instead of the propargyl group bound to the amine *N*-atom, in which the ligand adopts a *β*-cis folded conformation [32]. The electrochemical behavior of **1** in methanol is in agreement with the ESI-MS and conductivity results discussed above.

Due to its poor solubility in methanol, the electrochemical properties of complex **2** were studied in DMF. Within the potential window of DMF, the cyclic voltammogram of $\mathbf{2}^{2+}$ (Figure 5b) shows only two irreversible processes in the cathodic scan, at −1.27 and −1.40 V vs. *SCE*, assigned to the reduction of the Schiff base-pyridine conjugated system [63]. The complex is electrochemically inactive in the anodic scan, indicating a high stability of the Mn(II) center. It has been shown that the change of the *N*-donor site from tertiary amine to imine increases the Mn(III)/Mn(II) redox potential significantly [19,64]. Therefore, complex $\mathbf{2}^{2+}$ should be oxidized at a potential even higher than $[Mn(II)(pypapn)(OH_2)_2]^{2+}$.

Cyclic voltammogram of $\mathbf{3}^+$ displays a weakly reversible redox process at $E_{1/2}$ = 55 mV in methanol (Figure 5c) and a quasi-reversible process at $E_{1/2}$ = 142 mV in acetonitrile (Figure S5a,b), with ΔE = 0.13 V at scan rate = 0.1 V/s, corresponding to the Mn(III)/Mn(II) couple. The $E_{1/2}$ values correlate with the donor numbers (DN) of the solvents, $DN^{MeOH} = 19 > DN^{MeCN} = 14$, and evidence the solvent coordination to the metal center. The ratio of the current intensity of anodic and cathodic peaks, I_{pa}/I_{pc}, is 0.6 in methanol and 0.95 in acetonitrile, and the process is diffusion-controlled in acetonitrile (Figure S5c). In addition, the half width $w_{1/2}$ = 0.11 V observed by square-wave voltammetry (Figures 5c and S5a) confirms that the process is monoelectronic. The negative charge of the two phenolate groups in $[Mn(salbn)(solv)_2]^+$ results in significant stabilization of the Mn(III) oxidation state compared to the N_4-donor set in complexes $\mathbf{1}^{2+}$ and $\mathbf{2}^{2+}$. Given the difference in coordination geometry and radii requirements of the Mn(II) and Mn(III) ions, the chelate ring size is another factor that modulates the stability of the Mn oxidation state. Thereby, the Mn(III)/Mn(II) redox potentials of the $[Mn(III)(salen)(solv)_2]^+$ and $[Mn(III)(salpn)(solv)_2]^+$ analogues ($E_{1/2}$ = −0.225 V and −0.154 V, respectively) [57,58] are both more negative than $\mathbf{3}^+$ which possesses a longer and more flexible $–(CH_2)_4–$ spacer between the imine *N*-atoms that destabilizes the Mn(III) oxidation state with respect to reduction [65].

3.3. Synthesis and Characterization of Modified Mesoporous Silicas

SBA-15 and azide-modified mesoporous silica were used to immobilize the Mn complexes. Both silicas were synthesized employing tetraethyl orthosilicate (TEOS) as a Si source and the triblock copolymer Pluronic P-123 as the surfactant template. SBA-15 was prepared as previously described [19], affording an ordered mesoporous material (Figure S6) with a pore width of 5.2 nm and high specific surface area, calculated from the nitrogen adsorption-desorption isotherms at 77 K (Table 1, Figure 6). The azide functionalized mesoporous silica (N_3pn@OP-MS) was prepared by co-condensation of TEOS with 3-azidopropyltriethoxysilane (AzPTES) in the presence of the structural director agent Pluronic P-123. This "one-pot" method offers good control over the distribution of the

catalyst and has proven to favor a high proportion of organic groups covalently bound to the inner walls of the channels of the silica matrix [66], with the azidopropyl chains placed between the surfactant chains retaining the micellar assembling structure [67].

Table 1. Textural characterization of SBA-15 and N_3pn@OP-MS.

	S_{BET} ($m^2\ g^{-1}$)	$V_{\mu P}$ ($cm^3\ g^{-1}$)	V_{MP} ($cm^3\ g^{-1}$)	V_{TP} ($cm^3\ g^{-1}$)	w_P (nm)
SBA-15	568	0.06	0.51	0.63	5.2
N_3pn@OP-MS	362	0.00	0.41	0.47	4.8

$V_{TP} = V_{\mu P} + V_{primary\ MP} + V_{secondary\ MP}$, MP = mesopore; μP = micropore.

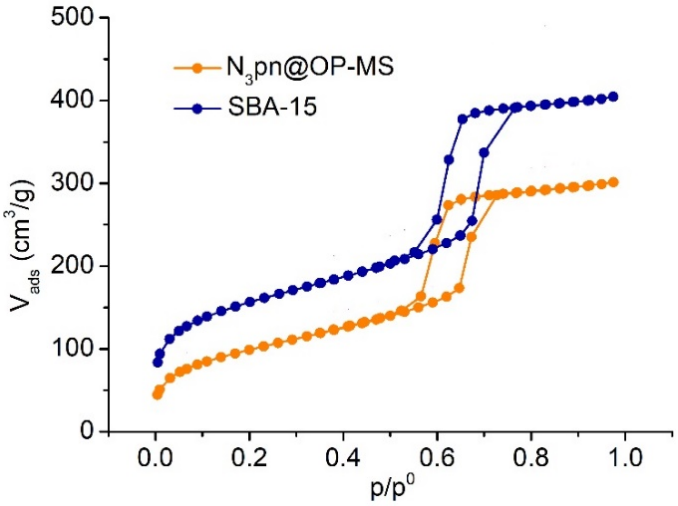

Figure 6. Adsorption-desorption N_2 isotherms of SBA-15 and N_3pn@OP-MS at 77 K.

The two materials display typical type IV isotherms with a sharp step and an H1 hysteresis loop at relative pressure p/p^0 = 0.5–0.7 [68] that evidences the azido functionalized material exhibits similar mesopore structure and uniform size distribution as SBA-15 (Figure 6). N_3pn@OP-MS possesses well-defined pores of similar diameter as SBA-15, although smaller volume and BET surface area (Table 1), as a consequence of the presence of the azidopropyl chains.

The pypapn ligand was covalently linked to N_3pn@OP-MS by "click" chemistry using $(Ph_3P)_3CuBr$ as catalyst [17], to yield pypntriazole@OP-MS. This reaction was monitored by IR until the azide band disappeared. Finally, the Mn complex was generated in situ by treatment of a suspension of pypntriazole@OP-MS with $MnCl_2$, yielding Mn-pypntriazole@OP-MS. Based on metal and nitrogen analyses, the ligand is likely to be attached to the pore walls at a single binding site as shown in Figure 7a.

Complexes $\mathbf{2}^{2+}$ and $\mathbf{3}^{+}$ were successfully introduced into the framework of SBA-15 silica through the ionic exchange, being retained inside the channels through electrostatic interactions with the negatively charged Si-O^- groups of the pores' surface. Therefore, the loading of the divalent complex cation $\mathbf{2}^{2+}$ is three times higher than monovalent $\mathbf{3}^{+}$. FT-IR spectra (not shown here) of the three hybrid materials show strong bands belonging to the Si-O-Si framework and silanol groups but no or negligible bands of functional groups of the complexes, meaning that the compounds are essentially located inside the pores.

Low-temperature X-band EPR spectra of Mn-pypntriazole@OP-MS and **2**@SBA-15 provide details on the geometry and coordination environment of the metal ions in the hybrid materials. The spectrum of the covalently anchored complex, Mn-pypntriazole@OP-MS, is dominated by a sextet at g_{eff} = 2.028 (hyperfine coupling of ≈ 90 G), and two additional transitions at g_{eff} ≈ 5.2 and 2.9 (Figure 7a). These spectral features are consistent with a high-spin Mn(II) complex with a *zfs* smaller than that of $[Mn(pypapn)Cl(H_2O)]^+$, denoting that inside the pores Mn is not bound to the chloride anion but to solvent molecules that

are ligands stronger than chloride and afford a distorted mononuclear Mn(II) center with reduced *zfs* [32]. This is probably the result of the lengthy preparation process during which the complex is in contact with the solvent. After encapsulation in SBA-15, $\mathbf{2}^{2+}$ retains the geometry of the complex in solution affording an EPR spectrum with a six-line signal centered at $g_{\text{eff}} \approx 2$, and two additional broad signals at $g_{\text{eff}} = 5.4$ and $g_{\text{eff}} = 2.8$ (Figure 7b) analogous to those observed in the EPR spectrum of the frozen DMSO solution of **2**.

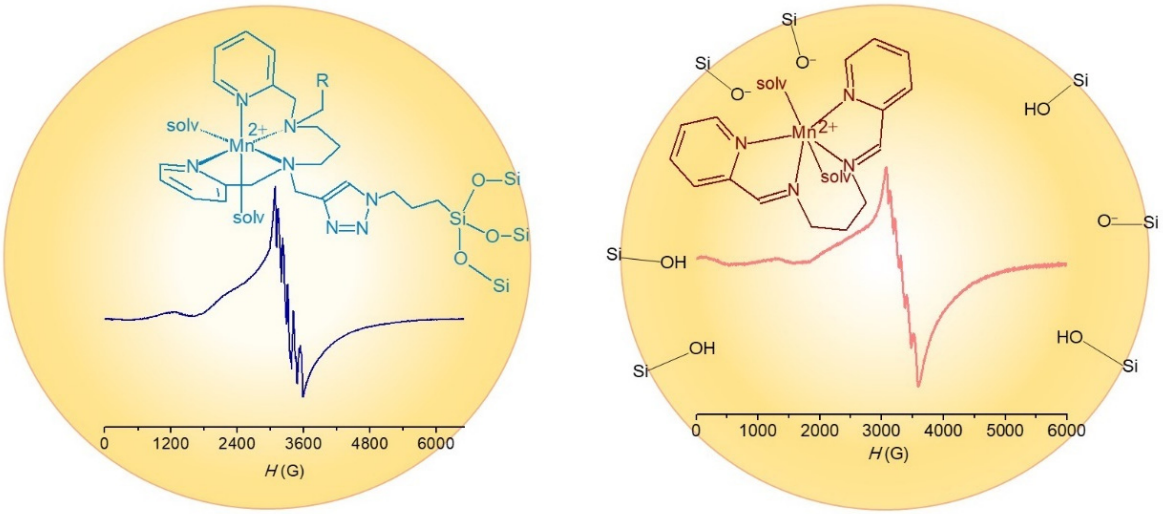

Figure 7. Low temperature X-band EPR spectra of complexes inside the pores. (**a**) Mn-pypntriazole@OP-MS and (**b**) **2**@SBA-15. T = 120 K, ν = 9.3 MHz.

The morphology and size of the particles of the hybrid materials were analyzed by scanning electron microscopy (SEM). SEM images of Mn-pypntriazole@OP-MS (Figure 8, left) show elongated particles of 0.8 ± 0.4 μm length and 0.5 ± 0.2 μm width, calculated from statistical analysis over 156 particles. **2**@SBA-15 and **3**@SBA-15 also show oblong particles (Figure 8, middle and right), lined up forming chains in the case of **3**@SBA-15, with an average length of 0.8 ± 0.3 μm and 1.0 ± 0.4 μm, respectively, and length to width ratio of 2 to 1 for both hybrid materials, calculated over 142 particles of **2**@SBA-15 and 95 of **3**@SBA-15.

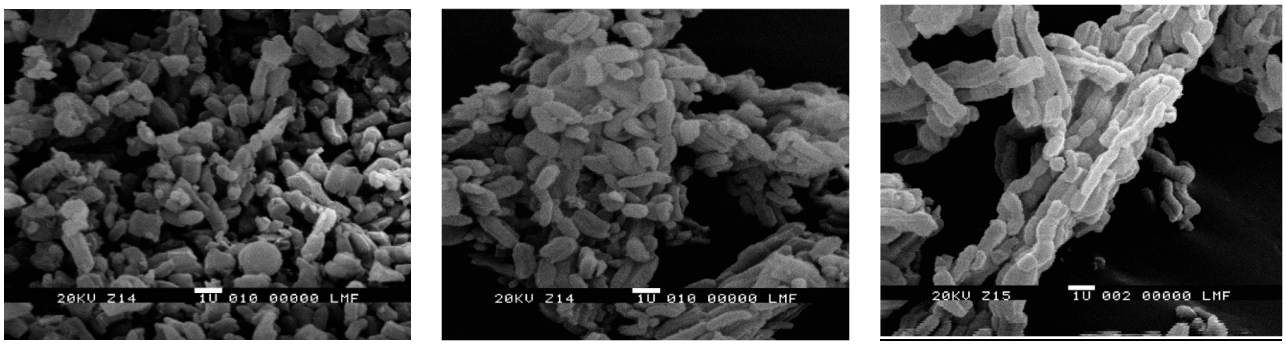

Mn-pypntriazole@OP-MS **2**@SBA-15 **3**@SBA-15

Figure 8. SEM images of the hybrid materials.

Transmission electron microscopy (TEM) images of the hybrid materials confirmed their highly ordered mesostructure, with a regular two-dimensional array of cylindrical channels in a hexagonal arrangement mostly parallel to the principal axes in all MSPs. Micrographs taken with the electron beam perpendicular to the pore direction show the

parallel channels crossing through the whole particles (Figure 9), while the highly ordered hexagonal mesoporous structure can be observed in the images taken when the electron beam is parallel to the channels (Figure S6).

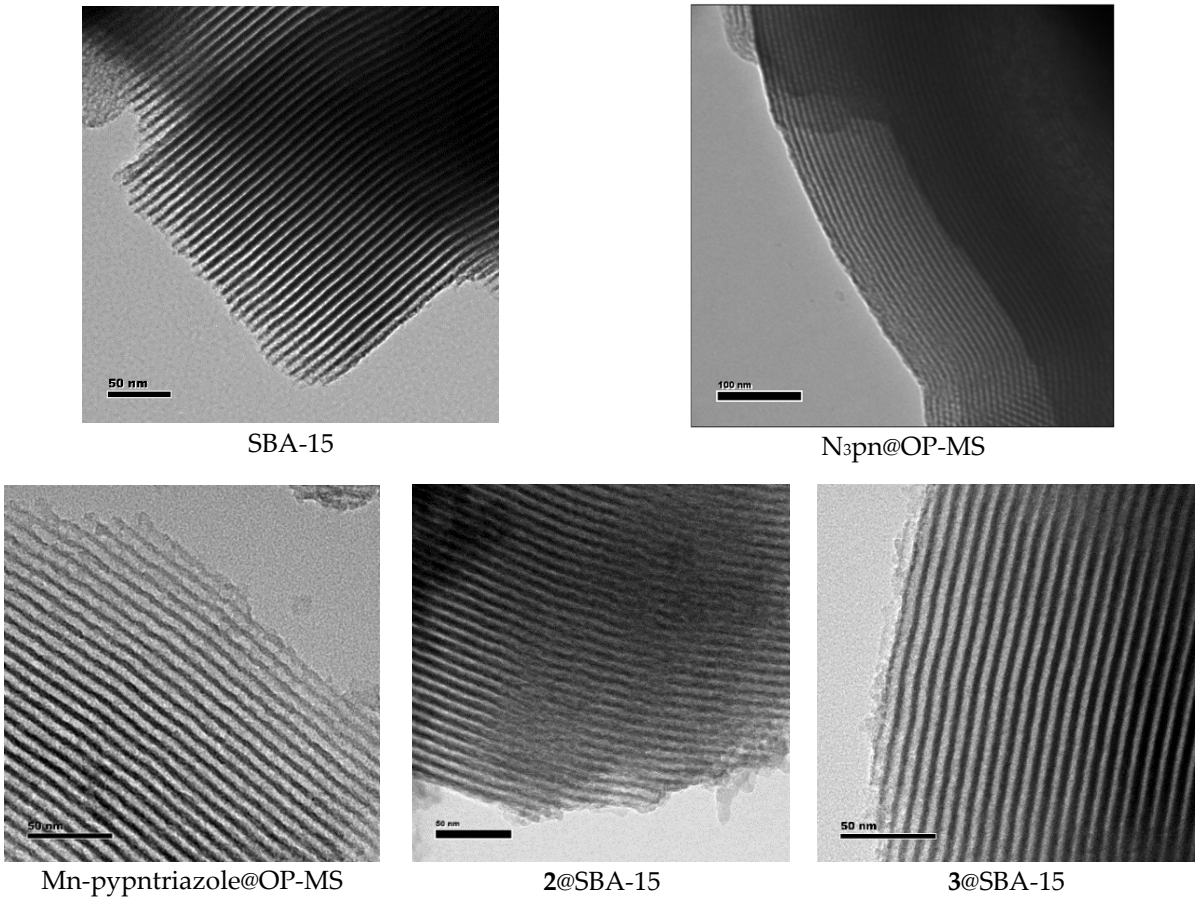

Figure 9. TEM images of the hybrid materials.

These results clearly demonstrate that covalent grafting of the complex to the pores wall or incorporation of the complexes inside the pores preserves the mesostructured ordering of the one-dimensional straight channels and hexagonal pores arrangement. In these materials, the pore network is exposed at the particle surface as an open porosity, an appropriate feature for the access of the substrate to interact with the catalyst. Pore diameter and wall thickness were calculated from statistical analysis of TEM images using a developed protocol that takes into account integration over grey scales in sample zones very carefully selected where the electron beam was aligned perpendicular to the channels. The average pore diameters are 4.7 ± 0.7 nm for Mn-pyrpntriazole@OP-MS, 5.1 ± 0.8 nm for **2**@SBA-15, and 4.3 ± 0.6 nm for **3**@SBA-15, with a wall thickness of 3.9 ± 0.6 nm, 3.3 ± 0.6 nm and 3.7 ± 0.5 nm, respectively.

3.4. SOD Activity

Prior to the SOD activity essays, the stability of the free and immobilized complexes in phosphate buffer was verified. UV–Vis spectra of the complexes $\mathbf{1}^{2+}$, $\mathbf{2}^{2+}$ and $\mathbf{3}^{+}$ registered after incubation in phosphate buffer of pH 7.8 for 2 h (Figure S7) showed constant spectral features and band intensities. Additionally, analysis of supernatant after centrifugation of suspensions of the hybrid materials incubated in phosphate buffer, evidenced the absence of complex leaching into the solution. Therefore, the activity of these materials, if any, must be due to the immobilized complex. The SOD activity of complexes $\mathbf{1}^{2+}$, $\mathbf{2}^{2+}$ and $\mathbf{3}^{+}$, and the hybrid materials, was measured by the Beauchamps and Fridovich indirect assay using

NBT in a phosphate buffer of pH 7.8 [27]. In this assay, the NBT and the catalyst compete for the photogenerated $O_2^{\bullet-}$, thereby the SOD activity is inversely related to the amount of formazan produced in the reaction of NBT with $O_2^{\bullet-}$, detected at 560 nm. The IC_{50}, the concentration of catalyst that diminishes by 50% the reduction of NBT by $O_2^{\bullet-}$, was determined from plots of % inhibition vs. [complex], and used to calculate the *McCord-Fridovich* second-order rate constants $k_{McF} = k_{NBT}$ [NBT]/IC_{50}, which are independent of the detector [28].

The three complexes have labile coordination positions to interact with the substrate and exhibit SOD activity (Figure 10). The k_{McF} and $E_{1/2}$ values for complexes $\mathbf{1}^{2+}$, $\mathbf{2}^{2+}$ and $\mathbf{3}^{+}$ are given in Table 2 and compared to other selected Mn complexes with *N/O*-tetradentate ligands (see Chart S1 for their structures) for which k_{McF} was reported or could be calculated from the IC_{50} values [14,19,58,69–75].

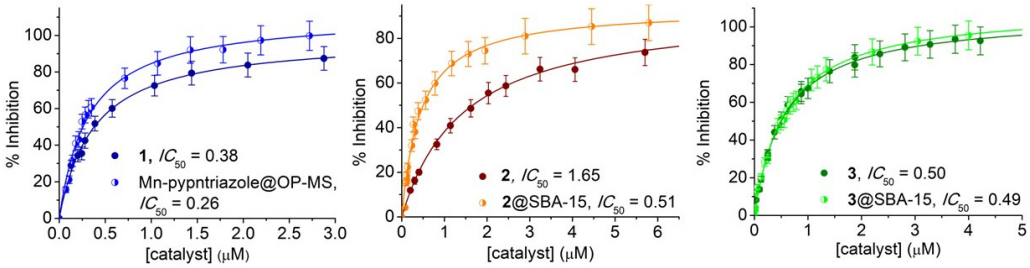

Figure 10. SOD activity of **1** and Mn-pypntriazole@OP-MS (**left**), **2** and **2**@SBA-15 (**middle**) and **3** and **3**@SBA-15 (**right**) in phosphate buffer of pH 7.8.

As can be observed, the Mn(II) complexes $\mathbf{1}^{2+}$ and $\mathbf{2}^{2+}$, with N_4-tetradentate ligands, show SOD activity despite the high potential of their Mn(III)/Mn(II) couple (entries 1 and 3, Table 2). This suggests these complexes react with $O_2^{\bullet-}$ through an inner-sphere electron-transfer mechanism, since for an outer-sphere one, the redox potential of the complex must be between the reduction and oxidation potentials of $O_2^{\bullet-}$. This is feasible because the $O_2^{\bullet-}$ nucleophilicity and the presence of labile water molecules coordinated to the metal center favor the formation of an adduct with superoxide followed by electron-transfer [76,77]. In such a mechanism, the SOD activity is also affected by the ligand flexibility to accommodate geometrical rearrangements when switching between Mn(II) and the Jahn-Teller distorted Mn(III) during catalysis. So, complex $\mathbf{1}^{2+}$ with the more flexible diamine ligand reacts faster than complex $\mathbf{2}^{2+}$ with the Schiff-base ligand, and even faster than [Mn(III)(bpb)Cl(H_2O)] (H_2bpb = *N*,*N*′-(1,2-phenylene)bis(pyridine-2-carboxamide), entry 4, Table 2) where the phenylene moiety between the *N*-amide donor sites confers rigidity to the complex. The Mn(II) complex of the tripodal amine NTB (NTB = tris(2-benzimidazolylmethyl)amine, entry 2, Table 2) that possesses an "open umbrella" shape, with the tertiary *N*-amine at the apex and terephthalate as the handle, reacts slower than $\mathbf{1}^{2+}$ owing to the steric hindrance of the binding N-atoms of the three benzimidazolyl groups laying in the equatorial plane of Mn(II).

Among the Mn(II) complexes of ligands bearing the N_3O-donor set (entries 5–8, Table 2), [Mn(II)(PClNOL)Cl_2] (PClNOL = 1-[bis(pyridin-2-ylmethyl)amino]-3-chloropropan-2-ol) stands out from [Mn(II)(PBMPA)Cl(H_2O)] and [Mn(II)(BMPG)(H_2O)]$^+$, even when the redox potential of the first is far away the midpoint of the reduction/oxidation potentials of $O_2^{\bullet-}$. Here also, an inner-sphere electron-transfer mechanism seems operative, where the apical Mn-O_{ol} bond in [Mn(II)(PClNOL)Cl_2] is weaker than the axial Mn-O_{CO2-} bond in [Mn(II)(PBMPA)Cl(H_2O)] and [Mn(II)(BMPG)(H_2O)]$^+$. Consequently, the strongest metal-ligand bonds weaken the Mn-superoxide bond and slower the SOD activity. This is even more evident when terminal pyridine groups of the tripodal amine ligands are replaced by benzimidazole groups in [Mn(II)(BIG)(H_2O)$_2$]$^+$, resulting in a drop of reactivity (entry 8, Table 2).

Table 2. SOD activity of **1–3** and other Mn complexes of tetradentate ligands.

Entry	Catalyst	Ligand Donor Sites	10^6 k_{McF} ($M^{-1}s^{-1}$)	$E_{1/2}$ (II/III) (V vs. SCE)	Ref.
1	$\mathbf{1}^{2+a}$	N_4	5.97	1.1 (E_{pa})	This work
2	[Mn(II)(NTB)(terphthalate)]	N_4	4.3	0.059	[69]
3	$\mathbf{2}^{2+}$	N_4	1.40	>1	This work
4	[Mn(III)(bpb)Cl(H_2O)]	N_4	0.93	−0.017	[70]
5	[Mn(II)(PClNOL)Cl_2]	N_3O	9.4	0.806	[71]
6	[Mn(II)(PBMPA)Cl(H_2O)]	N_3O	4.9	0.47	[72]
7	[Mn(II)(BMPG)(H_2O)]$^+$	N_3O	4.8	0.44 (E_{pa})	[73]
8	[Mn(II)(BIG)(H_2O)$_2$]$^+$	N_3O	1.5	0.756 (E_{pa})	[73]
9	$\mathbf{3}^{+}$	N_2O_2	4.54	0.055	This work
10	[Mn(III)(hbpapn)(H_2O)$_2$]$^+$	N_2O_2	3.90	0.42 (III/IV)	[19]
11	[Mn(III)(pyr$_2$pn)(H_2O)$_2$]$^+$	N_2O_2	1.84	ND	[74]
12	[Mn(III)(salpn)(H_2O)$_2$]$^+$	N_2O_2	1.53	−0.14	[58]
13	[Mn(III)(X-salen)(H_2O)$_2$]$^+$	N_2O_2	0.6	−0.237 to 0.031	[14,75]
14	MnSOD	N_3O	800	0.049	[2,78]
	Immobilized Catalyst		**10^6 k_{McF} (M^{-1} s^{-1})**		
15	Mn-pypntriazole@OP-MS		8.73		
16	**2**@SBA-15		4.45		
17	**3**@SBA-15		4.63		

NTB, tris(2-benzimidazolylmethyl)amine; H_2bpb, *N*,*N*′-(1,2-phenylene)bis(pyridine-2-carboxamide); HPClNOL, 1-[bis(pyridin-2-ylmethyl)amino]-3-chloropropan-2-ol; HPBMPA, N-propanoate-*N*,*N*-bis-(2-pyridylmethyl)amine; BMPG, *N*,*N*-bis[(6-methyl-2-pyridyl)methyl] glycinate; H_2pyr$_2$pn, 1,3-bis(pyridoxylidenamino)propane; salpn, 1,3-bis(salicylidenamino) propane; BIG, *N*,*N*-bis[(1-methyl-2-imidazolyl)methyl]glycinate; H_2hbpapn, 1,3-bis[(2-hydroxybenzyl)(propargyl)amino]propane; salen, *N*,*N*′-bis(salicylidene)-1,2-diaminoethane; X: aromatic substituents. [a] In the aqueous medium, [Mn(II)(pypapn)(H_2O)$_2$]$^{2+}$ ($\mathbf{1}^{2+}$) is proposed to form through Cl^-/water (DN^{H2O} = 33) ligand exchange.

In inner-sphere electron-transfer the ligand donor ability affects the Mn-O bond strength in the $[MnO_2]^+$ adduct and, consequently, the rate of $O_2^{\bullet-}$ dismutation. This becomes evident for Mn complexes of ligands with N_2O_2-donor set, with two phenolate donor sites, which react slowly despite having favorable redox potentials for $O_2^{\bullet-}$ dismutation, as exemplified by [Mn(salpn)]$^+$, [Mn(pyr$_2$pn)]$^+$ and [Mn(salen)]$^+$ in Table 2 (entries 11–13). In the case of complexes $\mathbf{3}^+$, with the longer and more flexible -$(CH_2)_4$- spacer between the imine functions (entry 9, Table 2), and [Mn(III)(hbpapn)(H_2O)$_2$]$^+$, with a more flexible diamine ligand adopting a folded disposition around Mn(III) (entry 10, Table 2), the higher donor ability of the phenolate groups is balanced by the lower ligand reorganization barrier when switching between Mn(II) and Mn(III) oxidation states, and, consequently, the SOD activity is higher than that of Mn-salpn and Mn-salen type complexes.

All the complexes in Table 2 are less active than the MnSOD enzyme (entry 14, Table 2), which contains a Mn ion bound to N_3(his)O(asp) donor sites of amino acid residues and one exogenous OH^- ion or a water molecule, arranged in a trigonal bipyramidal geometry [79]. The Mn site is surrounded by a hydrogen-bonded network comprising the side chains of several residues that presumably facilitates proton transfer during reduction and oxidation of $O_2^{\bullet-}$ and could account for the relative SOD activity of the enzyme compared to the complexes [2].

The ability of the hybrid materials to react with $O_2^{\bullet-}$ was evaluated (Figure 10) with the intention of checking the retention of the SOD activity upon immobilization of the three catalysts. The SOD activity of Mn-pypntriazole@OP-MS, with the complex covalently attached to the silica pores, is 1.5-times higher than $\mathbf{1}^{2+}$ in homogeneous phase (entry 15, Table 2), while encapsulation of [Mn(py$_2$pn)]$^{2+}$ ($\mathbf{2}^{2+}$) inside the pores of SBA-15 through ionic exchange, triples the SOD activity of the free complex (entry 16, Table 2). The significant enhancement of activity of **2**@SBA-15 is probably related to the increased distortion of the complex upon reaction with KO_2 inside the pores, as could be confirmed

by low-temperature X-band EPR spectroscopy of the hybrid material after the reaction with KO_2 in DMSO (Figure S8, left). Unlike **2**@SBA-15, EPR spectra registered before and after reaction of Mn-pypntriazole@OP-MS with KO_2 in DMSO are analogous. **3**@SBA-15 is EPR silent, but after reaction with KO_2 gives a very low intensity Mn(II) signal, as shown in Figure S8 (right), suggesting the reaction involves Mn(II)/Mn(III) oxidation states. The absence of the signal characteristic of superoxide in the EPR spectra registered after addition of the hybrid materials to a DMSO solution containing 10-times excess of KO_2, confirmed that these materials act as catalysts for $O_2^{\bullet-}$ dismutation. To verify if the activity is retained after several cycles, the NBT conversion was measured after successive illuminations of the reaction mixture with and without the hybrid material. In each new illumination, the NBT concentration was kept constant by the addition of the required amount of NBT to restore the initial concentration. Mn-pypntriazole@OP-MS and **2**@SBA-15 retain the activity after several illumination cycles, denoting the stability of the coated catalysts. The enhanced stability of the immobilized catalysts can be interpreted as the result of the confinement effect of the mesoporous material that plays a role similar to that of the enzyme backbone in protecting the active site from reacting with superoxide. Encapsulated $[Mn(salbn)(solv)_2]^+$ keeps the reactivity of the homogeneous catalyst in the first cycle (entry 17, Table 2, Figure 10, right panel). However, after successive illuminations, **3**@SBA-15 gradually loses activity due to catalyst leakage from the mesoporous matrix, probably because the neutral reduced form of this complex, $[Mn(II)(salbn)(solv)_2]$, is poorly retained by the silica, as already observed for the Mn-salpn system [19]. Therefore, the charge of the Mn complex inside the silica matrix is essential to achieve a long-lived and reusable catalyst.

4. Conclusions

Despite the high potential of the Mn(III)/Mn(II) couple, Mn(II) complexes formed with the N_4-tetradentate ligands pypapn ($\mathbf{1}^{2+}$) and py_2pn ($\mathbf{2}^{2+}$) show SOD activity in aqueous phosphate buffer of pH 7.8, suggesting these complexes react with $O_2^{\bullet-}$ through an inner-sphere electron-transfer mechanism. The Mn(III) complex of the N_2O_2-tetradentate $salbn^{2-}$ ($\mathbf{3}^{+}$) that has a redox potential closer to the midpoint between $O_2^{\bullet-}$ reduction/oxidation potentials, reacts with $O_2^{\bullet-}$ at a similar rate as $\mathbf{1}^{2+}$ and faster than other complexes with more rigid N_2O_2-Schiff base ligands and similar redox potentials. Therefore, Mn complexes with more flexible ligands, such as pypapn and $salbn^{2-}$, react faster than those of more rigid ones, because the ligand can rearrange more easily during switching between Mn(II) and Mn(III) oxidation states. Ultimately, ligand flexibility appears as a much more critical feature than the redox potential of the metal center when the reaction occurs through an inner-sphere electron-transfer mechanism. Either covalent grafting or encapsulation of the catalysts has shown a positive impact on the SOD activity, implying that the catalytic conversion is not hindered by diffusion of the substrate through the silica nanochannels. The retention or enhancement of the catalytic activity of the hybrid materials compared to the free catalysts, and the improved stability of the covalently attached catalyst ($\mathbf{1}^{2+}$) and the doubly charged complex encapsulated in the silica pores ($\mathbf{2}^{2+}$), make them suitable for use in aqueous media.

Supplementary Materials: The following supporting information can be downloaded at: https://www.mdpi.com/article/10.3390/inorganics11090359/s1, Spectroscopic data for py_2pn and H_2salbn; Figure S1: ^1H and ^{13}C NMR spectra of pypapn in $CDCl_3$; Figure S2: FT-IR spectra of pypapn and complex **1** and ^1H NMR spectrum of **1** in D_4-methanol; Figure S3: FT-IR spectra of py_2pn and complex **2**, electronic spectrum of **2** in acetonitrile, positive ESI-mass spectrum of **2** in MeOH; Figure S4: ^1H NMR spectrum of H_2salbn in $CDCl_3$ and FT-IR spectrum of **3**; Figure S5: Cyclic and square wave voltammogram of **3** in acetonitrile and I_{pa} (and I_{pc}) vs. $r^{1/2}$ plot; Figure S6: TEM images of mesoporous materials; Figure S7: Electronic spectra of **1**, **2** and **3** in phosphate buffer of pH 7.8 after 2 h of incubation; Figure S8: X-band EPR spectra of **2**@SBA-15 and **3**@SBA-15 after reaction with KO_2 in DMSO; Chart S1: Structures of complexes listed in Table 2.

Author Contributions: Conceptualization, S.R.S. and C.P.; Methodology, Resources, Funding Acquisition, S.R.S., C.P., N.P. and C.H.; Investigation, M.R., S.S. and N.P.; Formal Analysis, M.R., S.S., S.R.S. and N.P.; Writing—Original Draft Preparation, S.R.S.; Writing—Review & Editing, S.R.S., C.H., N.P. and C.P.; Supervision, S.R.S. and C.P. All authors have read and agreed to the published version of the manuscript.

Funding: This research was funded by National University of Rosario (PIP-BIO553, PIP-BIO483 and PID 8002019040023UR), Consejo Nacional de Investigaciones Científicas y Técnicas (CONICET, PIP-0852 and PUE-0068), Centre National de la Recherche Scientifique (CNRS, PICS-07121), and Agencia Nacional de Promoción Científica y Tecnológica (ANPCyT, PICT-2019-03276).

Data Availability Statement: The data presented in this study are available on request from the corresponding author.

Conflicts of Interest: The authors declare no conflict of interest. The funders had no role in the design of the study.

References

1. Yang, B.; Chen, Y.; Shi, J. Reactive Oxygen Species (ROS)-Based Nanomedicine. *Chem. Rev.* **2019**, *119*, 4881–4985.
2. Sheng, Y.; Abreu, I.A.; Cabelli, D.E.; Maroney, M.J.; Miller, A.-F.; Teixeira, M.; Valentine, J.S. Superoxide Dismutases and Superoxide Reductases. *Chem. Rev.* **2014**, *114*, 3854–3918.
3. Dixon, M.M.; Pattridge, K.A.; Stallings, W.C.; Fee, J.A.; Ludwig, M.L. Structure—Function in *Escherichia coli* Iron Superoxide Dismutase: Comparisons with the Manganese Enzyme from *Thermus thermophilus*. *Biochemistry* **1995**, *34*, 1646–1660.
4. Sayre, L.M.; Perry, G.; Smith, M.A. Oxidative Stress and Neurotoxicity. *Chem. Res. Toxicol.* **2008**, *21*, 172–188.
5. Salvemini, D.; Muscoli, C.; Riley, D.P.; Cuzzocrea, S. Superoxide Dismutase Mimetics. *Pulm. Pharmacol. Ther.* **2002**, *15*, 439–447.
6. Miriyala, S.; Spasojevic, I.; Tovmasyan, A.; Salvemini, D.; Vujaskovic, Z.; St. Clair, D.; Batinic-Haberle, I. Manganese superoxide dismutase, MnSOD and its mimics. *Biochim. Biophys. Acta* **2012**, *1822*, 794–814.
7. Bonetta, R. Potential Therapeutic Applications of MnSODs and SOD-Mimetics. *Chem. Eur. J.* **2018**, *24*, 5032–5041. [CrossRef]
8. Policar, C.; Bouvet, J.; Bertrand, H.C.; Delsuc, N. SOD mimics: From the toolbox of the chemists to cellular studies. *Curr. Opin. Chem. Biol.* **2022**, *67*, 102109. [CrossRef]
9. Signorella, S.; Palopoli, C.; Ledesma, G. Rationally designed mimics of antioxidant manganoenzymes: Role of structural features in the quest for catalysts with catalase and superoxide dismutase activity. *Coord. Chem. Rev.* **2018**, *365*, 75–102.
10. Schanne, G.; Zoumpoulaki, M.; Gazzah, G.; Vincent, A.; Preud'Homme, H.; Lobinski, R.; Demignot, S.; Seksik, P.; Delsuc, N.; Policar, C. Inertness of Superoxide Dismutase Mimics Mn(II) Complexes Based on an Open-Chain Ligand, Bioactivity, and Detection in Intestinal Epithelial Cells. *Oxidative Med. Cell. Longev.* **2022**, *2022*, 3858122.
11. Garda, Z.; Molnár, E.; Hamon, N.; Barriada, J.L.; Gómez, D.E.; Váradi, B.; Nagy, V.; Pota, K.; Kálmán, F.K.; Tóth, I.; et al. Complexation of Mn(II) by Rigid Pyclen Diacetates: Equilibrium, Kinetic, Relaxometric, Density Functional Theory, and Superoxide Dismutase Activity Studies. *Inorg. Chem.* **2021**, *60*, 1133–1148. [CrossRef] [PubMed]
12. Mathieu, E.; Bernard, A.-S.; Delsuc, N.; Quévrain, E.; Gazzah, G.; Lai, B.; Chain, F.; Langella, P.; Bachelet, M.; Masliah, J.; et al. A Cell-Penetrant Manganese Superoxide Dismutase (MnSOD) Mimic Is Able To Complement MnSOD and Exerts an Antiinflammatory Effect on Cellular and Animal Models of Inflammatory Bowel Diseases. *Inorg. Chem.* **2017**, *56*, 2545–2555. [CrossRef] [PubMed]
13. Kálmán, F.K.; Tircsó, G. Kinetic Inertness of the Mn^{2+} Complexes Formed with AAZTA and Some Open-Chain EDTA Derivatives. *Inorg. Chem.* **2012**, *51*, 10065–10067. [CrossRef]
14. González-Riopedre, G.; Fernández-García, M.; Gómez-Fórneas, E.; Maneiro, M. Biomimetic Catalysts for Oxidation of Veratryl Alcohol, a Lignin Model Compound. *Catalysts* **2013**, *3*, 232–246.
15. Mureseanu, M.; Filip, M.; Bleotu, I.; Spinu, C.I.; Marin, A.H.; Matei, I.; Parvulescu, V. Cu(II) and Mn(II) Anchored on Functionalized Mesoporous Silica with Schiff Bases: Effects of Supports and Metal–Ligand Interactions on Catalytic Activity. *Nanomaterials* **2023**, *13*, 1884. [CrossRef] [PubMed]
16. Rana, B.S.; Jain, S.L.; Singh, B.; Bhaumik, A.; Sain, B.; Sinha, A.K. Click on silica: Systematic immobilization of Co(II)Schiff bases to the mesoporous silicavia click reaction and their catalytic activity for aerobic oxidation of alcohols. *Dalton Trans.* **2010**, *39*, 7760–7767. [CrossRef]
17. Chaignon, J.; Stiriba, S.-E.; Lloret, F.; Yuste, C.; Pilet, G.; Bonneviot, L.; Albela, B.; Castro, I. Bioinspired manganese(II) complexes with a clickable ligand for immobilisation on a solid support. *Dalton Trans.* **2014**, *43*, 9704–9713. [CrossRef]
18. Nodzewska, A.; Wadolowska, A.; Watkinson, M. Recent advances in the catalytic oxidation of alkene and alkane substrates using immobilized manganese complexes with nitrogen containing ligands. *Coord. Chem. Rev.* **2019**, *382*, 181–216.
19. Richezzi, M.; Palopoli, C.; Pellegri, N.; Hureau, C.; Signorella, S.R. Synthesis, characterization and superoxide dismutase activity of a biomimetic Mn(III) complex covalently anchored to mesoporous silica. *J. Inorg. Biochem.* **2022**, *237*, 112026. [CrossRef]
20. Liberman, A.; Mendez, N.; Trogler, W.C.; Kummel, A.C. Synthesis and surface functionalization of silica nanoparticles for nanomedicine. *Surf. Sci. Rep.* **2014**, *69*, 132–158.

21. Sun, R.; Qiao, P.; Wang, Z.; Wang, W. Monodispersed large-mesopore mesoporous silica nanoparticles enabled by sulfuric acid assisted hydrothermal process. *Microporous Mesoporous Mater.* **2021**, *317*, 111023. [CrossRef]
22. Ebralidze, I.I.; Leitus, G.; Shimon, L.J.W.; Wang, Y.; Shaik, S.; Neumann, R. Structural variability in manganese(II) complexes of N,N′-bis(2-pyridinylmethylene) ethane (and propane) diamine ligands. *Inorg. Chim. Acta* **2009**, *362*, 4713–4720. [CrossRef]
23. Kadwa, E.; Bala, M.D.; Friedrich, H.B. Characterisation and application of montmorillonite-supported Fe Schiff base complexes as catalysts for the oxidation of n-octane. *Appl. Clay Sci.* **2014**, *95*, 340–347. [CrossRef]
24. Thielemann, J.P.; Girgsdies, F.; Schlögl, R.; Hess, C. Pore structure and surface area of silica SBA-15: Influence of washing and scale-up. *Beilstein J. Nanotechnol.* **2011**, *2*, 110–118. [CrossRef]
25. Thommes, M.; Kaneko, K.; Neimark, A.V.; Olivier, J.P.; Rodriguez-Reinoso, F.; Rouquerol, J.; Sing, K.S.W. Physisorption of gases, with special reference to the evaluation of surface area and pore size distribution (IUPAC Technical Report). *Pure Appl. Chem.* **2015**, *87*, 1051–1069. [CrossRef]
26. Villarroel Rocha, J.; Barrera, D.; Sapag, K. Improvement in the Pore Size Distribution for Ordered Mesoporous Materials with Cylindrical and Spherical Pores Using the Kelvin Equation. *Top. Catal.* **2011**, *54*, 121–134. [CrossRef]
27. Beauchamps, C.; Fridovich, I. Superoxide dismutase: Improved assays and an assay applicable to acrylamide gels. *Anal. Biochem.* **1971**, *44*, 276–287. [CrossRef]
28. Liao, Z.-R.; Zheng, X.-F.; Luo, B.-S.; Shen, L.-R.; Li, D.-F.; Liu, H.-L.; Zhao, W. SOD-like activities of manganese-containing complexes with N,N,N,N-tetrakis(2-benzimidazolyl methyl)-1,2-ethanediamine (EDTB). *Polyhedron* **2001**, *20*, 2813–2821. [CrossRef]
29. Hyland, K.; Auclair, C. The formation of superoxide radical anions by a reaction between O_2, OH^- and dimethyl sulfoxide. *Biochem. Biophys. Res. Commun.* **1981**, *102*, 531–537. [CrossRef]
30. Dowsing, R.D.; Nieuwenhuijse, B.; Reedijk, J. Pyrazoles and imidazoles as ligands. X. electron paramagnetic resonance spectra of MnII in a tetragonal environment of four pyrazoles and two anions. *Inorg. Chim. Acta* **1971**, *5*, 301–304. [CrossRef]
31. Warzeska, S.T.; Miccichè, F.; Mimmi, M.C.; Bouwman, E.; Kooijman, H.; Spek, A.L.; Reedijk, J. Tuning the coordination mode in mononuclear manganese complexes by changing the steric bulk of the carboxylates. *J. Chem. Soc. Dalton Trans.* **2001**, 3507–3512. [CrossRef]
32. Hureau, C.; Blondin, G.; Charlot, M.-F.; Philouze, C.; Nierlich, M.; Césario, M.; Anxolabéhère-Mallart, E. Synthesis, Structure, and Characterization of New Mononuclear Mn(II) Complexes. Electrochemical Conversion into New Oxo-Bridged Mn2(III,IV) Complexes. Role of Chloride Ions. *Inorg. Chem.* **2005**, *44*, 3669–3683. [CrossRef] [PubMed]
33. Duboc, C.; Collomb, M.-N.; Neese, F. Understanding the Zero-Field Splitting of Mononuclear Manganese(II) Complexes from Combined EPR Spectroscopy and Quantum Chemistry. *Appl. Magn. Reson.* **2010**, *37*, 229–245. [CrossRef]
34. Jabłonska-Wawrzycka, A.; Barszcz, B.; Zienkiewicz, M.; Hodorowicz, M.; Jezierska, J.; Stadnicka, K.; Lechowicz, Ł.; Kaca, W. Eight- and six-coordinated Mn(II) complexes of heteroaromatic alcohol and aldehyde: Crystal structure, spectral, magnetic, thermal and antibacterial activity studies. *Spectrochim. Acta Part A* **2014**, *129*, 632–642. [CrossRef] [PubMed]
35. Duboc, C.; Phoeung, T.; Zein, S.; Pécaut, J.; Collomb, M.N.; Neese, F. Origin of the Zero-Field Splitting in Mononuclear Octahedral Dihalide MnII Complexes: An Investigation by Multifrequency High-Field Electron Paramagnetic Resonance and Density Functional Theory. *Inorg. Chem.* **2007**, *46*, 4905–4916. [CrossRef] [PubMed]
36. Mantel, C.; Baffert, C.; Romero, I.; Deronzier, A.; Pécaut, J.; Collomb, M.-N.; Duboc, C. Structural Characterization and Electronic Properties Determination by High-Field and High-Frequency EPR of a Series of Five-Coordinated Mn(II) Complexes. *Inorg. Chem.* **2004**, *43*, 6455–6463. [CrossRef]
37. Duboc, C. Determination and prediction of the magnetic anisotropy of Mn ions. *Chem. Soc. Rev.* **2016**, *45*, 5834–5847. [CrossRef]
38. Bucher, C.; Duval, E.; Barbe, J.-M.; Verpeaux, J.-N.; Amatore, C.; Guilard, R.; Le Pape, L.; Latour, J.-M.; Dahaoui, S.; Lecomte, C. Synthesis, X-ray Structure, Electrochemical, and EPR Studies of a Pentacoordinated Mn(II) Tetramethylcyclam Complex. *Inorg. Chem.* **2001**, *40*, 5722–5726. [CrossRef]
39. Hureau, C.; Groni, S.; Guillot, R.; Blondin, G.; Duboc, C.; Anxolabéhère-Mallart, E. Syntheses, X-ray Structures, Solid State High-Field Electron Paramagnetic Resonance, and Density-Functional Theory Investigations on Chloro and Aqua MnII Mononuclear Complexes with Amino-Pyridine Pentadentate Ligands. *Inorg. Chem.* **2008**, *47*, 9238–9247. [CrossRef]
40. Ali, I.; Wani, W.A.; Saleem, K. Empirical Formulae to Molecular Structures of Metal Complexes by Molar Conductance. *Synth. React. Inorg. Met.-Org. Chem.* **2013**, *43*, 1162–1170. [CrossRef]
41. Conradie, J.; Conradie, M.M.; Tawfiq, K.M.; Al-Jeboori, M.J.; Coles, S.J.; Wilson, C.; Potgieter, J.H. Novel dichloro(bis{2-[1-(4-methylphenyl)-1H-1,2,3-triazol-4-yl-κN3]pyridine-κN})metal(II) coordination compounds of seven transition metals (Mn, Fe, Co, Ni, Cu, Zn and Cd). *Polyhedron* **2018**, *151*, 243–254. [CrossRef]
42. Farkas, D.; Hansson, Ö. An NMR study elucidating the binding of Mg(II) and Mn(II) to spinach plastocyanin. Regulation of the binding of plastocyanin to subunit PsaF of photosystem I. *Biochim. Biophys. Acta (BBA)-Bioenerg.* **2011**, *1807*, 1539–1548. [CrossRef] [PubMed]
43. Sultana, N.; Arayne, M.S.; Rizvi, S.B.S.; Haroon, U.; Mesaik, M.A. Synthesis, spectroscopic, and biological evaluation of some levofloxacin metal complexes. *Med. Chem. Res.* **2013**, *22*, 1371–1377. [CrossRef]
44. Lavanant, H.; Virelizier, H.; Hoppilliard, Y. Reduction of Copper (II) Complexes by Electron Capture in an Electrospray Ionization Source. *J. Am. Soc. Mass Spectrom.* **1998**, *9*, 1217–1221. [CrossRef]
45. Dikio, C.W.; Ejidike, I.P.; Mtunzi, F.M.; Klink, M.J.; Dikio, E.D. Hydrazide schiff bases of acetylacetonate metal complexes: Synthesis, spectroscopic and biological studies. *Int. J. Pharm. Pharm. Sci.* **2017**, *9*, 257–267. [CrossRef]

46. Jambulingam, M.; Thangadurai, S.A.; Vijayabaskaran, M. Designing and Synthesis of Some Transition Metal Complexes Derived from Schiff Bases for Anti-Bacterial Activity. *J. Med. Chem. Sci.* **2022**, *5*, 10–18.
47. Kanumfre, F.; de Lima, E.M.; Scheidt, G.; Carneiro, P.I.B.; Rosso, N.D. Potentiometric and spectrophotometric studies of Mn^{II} and Ni^{II} cimetidine complexes. *J. Braz. Chem. Soc.* **2010**, *21*, 800–805. [CrossRef]
48. Biswas, S.; Mitra, K.; Adhikary, B. Studies on binuclear hydroxo/carboxylato-bridged manganese (III) complexes and a mononuclear manganese (III) complex involving salen type ligands. *Transit. Met. Chem.* **2005**, *30*, 586–592. [CrossRef]
49. Zhou, H.-B.; Wang, H.-S.; Chen, Y.; Xu, Y.-L.; Song, X.-J.; Song, Y.; Zhang, Y.-Q.; You, X.Z. Synthesis, structure, magnetic properties and DFT calculations of two hydroxo-bridged complexes based on Mn^{III} (Schiff-Bases). *Dalton Trans.* **2011**, *40*, 5999–6006. [CrossRef] [PubMed]
50. Mundlapati, V.R.; Jena, P.; Acharya, A.N.; Kar, A.K.; Dash, A.C.; Biswal, H.S. Water exchange reaction of a manganese catalase mimic: Oxygen-17 NMR relaxometry study on (aqua)manganese(III) in a salen scaffold and its reactions in a mildly basic medium. *RSC Adv.* **2016**, *6*, 111739–111746. [CrossRef]
51. Kurahashi, T. Reverse catalase reaction: Dioxygen activation via two-electron transfer from hydroxide to dioxygen mediated by a manganese(III) salen complex. *Inorg. Chem.* **2015**, *54*, 8356–8366. [CrossRef] [PubMed]
52. Si, S.F.; Tang, J.K.; Liao, D.Z.; Jiang, Z.H.; Yan, S.P. Synthesis and crystal structure of oxo-bridged dimanganese(III) complex $[Mn^{III}(salpn)OH]_2(CH_3OH)(CH_3CN)_2$. *J. Mol. Struct.* **2002**, *606*, 87–90. [CrossRef]
53. Chu, H.-A.; Hillier, W.; Law, N.A.; Babcock, G.T. Vibrational spectroscopy of the oxygen-evolving complex and of manganese model compounds. *Biochim. Biophys. Acta* **2001**, *1503*, 69–82. [CrossRef] [PubMed]
54. Bonadies, J.A.; Maroney, M.J.; Pecoraro, V.L. Structurally diverse manganese(III) Schiff base complexes: Solution speciation via paramagnetic proton NMR spectroscopy and electrochemistry. *Inorg. Chem.* **1989**, *28*, 2044–2051. [CrossRef]
55. Larson, E.J.; Pecoraro, V.L. The peroxide-dependent. μ_2-O bond formation of manganese complex $[Mn^{IV}$ SALPN(O)$]_2$. *J. Am. Chem. Soc.* **1991**, *113*, 3810–3818. [CrossRef]
56. Hoogenraad, M.; Ramkisoensing, K.; Driessen, W.L.; Kooijman, H.; Spek, A.L.; Bouwman, E.; Haasnoot, J.G.; Reedijk, J. Catalytic and electrochemical properties of new manganese(III) compounds of 2-(2′-hydroxyphenyl)-oxazoline (Hphox or HClphox). Molecular structures of $[Mn(Clphox)_2(MeOH)_2](ClO_4)$ and $[Mn(phox)_2(MeOH)_2][Mn(phox)_2(ClO_4)_2](H_2O)_2$. *Inorg. Chim. Acta* **2001**, *320*, 117–126. [CrossRef]
57. Palopoli, C.; Gómez, G.; Foi, A.; Doctorovich, F.; Mallet-Ladeira, S.; Hureau, C.; Signorella, S. Dimerization, redox properties and antioxidant activity of two manganese (III) complexes of difluoro-and dichloro-substituted Schiff-base ligands. *J. Inorg. Biochem.* **2017**, *167*, 49–59. [CrossRef]
58. Palopoli, C.; Ferreyra, J.; Conte-Daban, A.; Richezzi, M.; Foi, A.; Doctorovich, F.; Anxolabéhère-Mallart, E.; Hureau, C.; Signorella, S.R. Insights into Second-Sphere Effects on Redox Potentials, Spectroscopic Properties, and Superoxide Dismutase Activity of Manganese Complexes with Schiff-Base Ligands. *ACS Omega* **2019**, *4*, 48–57. [CrossRef]
59. Torayama, H.; Nishide, T.; Asada, H.; Fujiwara, M.; Matsushita, T. Preparation and characterization of different two types of di-μ-oxo dimanganese (IV) complexes with tetradentate Schiff bases. *Polyhedron* **1998**, *17*, 105–118. [CrossRef]
60. El Ghachtouli, S.; Ching, H.Y.V.; Lassalle-Kaiser, B.; Guillot, R.; Leto, D.F.; Chattopadhyay, S.; Jackson, T.A.; Dorlet, P.; Anxolabéhère-Mallart, E. Electrochemical formation of Mn III-peroxo complexes supported by pentadentate amino pyridine and imidazole ligands. *Chem. Commun.* **2013**, *49*, 5696–5698. [CrossRef]
61. Singh, O.; Maji, A.; Singh, A.; Singh, N.; Ghosh, K. A new family of complexes derived from bis (imino) pyridine-type ligands: Crystal structures and bio-molecular interaction studies. *Appl. Organomet. Chem.* **2021**, *35*, e6177. [CrossRef]
62. Rich, J.; Manrique, E.; Molton, F.; Duboc, C.; Collomb, M.-N.; Rodríguez, M.; Romero, I. Catalytic Activity of Chloro and Triflate Manganese(II) Complexes in Epoxidation Reactions: Reusable Catalytic Systems for Alkene Epoxidation. *Eur. J. Inorg. Chem.* **2014**, *2014*, 2663–2670. [CrossRef]
63. Adhikary, J.; Chakraborty, A.; Dasgupta, S.; Chattopadhyay, S.K.; Kruszynski, R.; Trzesowska-Kruszynska, A.; Stepanović, S.; Gruden-Pavlović, M.; Swart, M.; Das, D. Unique mononuclear Mn^{II} complexes of an end-off compartmental Schiff base ligand: Experimental and theoretical studies on their bio-relevant catalytic promiscuity. *Dalton Trans.* **2016**, *45*, 12409–12422. [PubMed]
64. Melville, J.N.; Bernhardt, P.V. Electrochemical Exploration of Active Cu-Based Atom Transfer Radical Polymerization Catalysis through Ligand Modification. *Inorg. Chem.* **2021**, *60*, 9709–9719. [CrossRef] [PubMed]
65. Signorella, S.; Hureau, C. Bioinspired functional mimics of the manganese catalases. *Coord. Chem. Rev.* **2012**, *256*, 1229–1245. [CrossRef]
66. Malvi, B.; Sarkar, B.R.; Pati, D.; Mathew, R.; Ajithkumarb, T.G.; Sen Gupta, S. "Clickable" SBA-15 mesoporous materials: Synthesis, characterization and their reaction with alkynes. *J. Mater. Chem.* **2009**, *19*, 1409–1416. [CrossRef]
67. Mercier, L.; Pinnavaia, T.J. Direct Synthesis of Hybrid Organic−Inorganic Nanoporous Silica by a Neutral Amine Assembly Route: Structure−Function Control by Stoichiometric Incorporation of Organosiloxane Molecules. *Chem. Mater.* **2000**, *12*, 188–196. [CrossRef]
68. Sing, K.S.W. Reporting physisorption data for gas/solid systems with special reference to the detemination of surface area and porosity. *Pure Appl. Chem.* **1985**, *57*, 603–619. [CrossRef]
69. Xiang, D.F.; Tan, X.S.; Hang, Q.W.; Tang, W.X.; Wu, B.-M.; Mak, T.C.W. Crystal structure and properties of a new five-coordinate manganese superoxide dismutase mimic. *Inorg. Chim. Acta* **1998**, *277*, 21–25.

70. Lin, J.; Tu, C.; Lin, H.; Jiang, P.; Ding, J.; Guo, Z. Crystal structure and superoxide dismutase activity of a six-coordinate manganese (III) complex. *Inorg. Chem. Commun.* **2003**, *6*, 262–265. [CrossRef]
71. Ribeiro, T.P.; Fernandes, C.; Melo, K.V.; Ferreira, S.S.; Lessa, J.A.; Franco, R.W.A.; Schenk, G.; Pereira, M.D.; Horn, A., Jr. Iron, copper and manganese complexes with in vitro superoxide dismutase and/or catalase activities that keep *Saccharomyces cerevisiae* cells alive under severe oxidative stress. *Free Radical Biol. Med.* **2015**, *80*, 67–76. [CrossRef] [PubMed]
72. Pap, J.S.; Kripli, B.; Bors, I.; Bogáth, D.; Giorgi, M.; Kaizer, J.; Speier, G. Transition metal complexes bearing flexible N_3 or N_3O donor ligands: Reactivity toward superoxide radical anion and hydrogen peroxide. *J. Inorg. Biochem.* **2012**, *117*, 60–70. [CrossRef]
73. Durot, S.; Policar, C.; Cisnetti, F.; Lambert, F.; Renault, J.; Pelosi, G.; Blain, G.; Korri-Youssoufi, H.; Mahy, J. Series of Mn Complexes Based on N-Centered Ligands and Superoxide—Reactivity in an Anhydrous Medium and SOD-Like Activity in an Aqueous Medium Correlated to Mn^{II}/Mn^{iii} Redox Potentials. *Eur. J. Inorg. Chem.* **2005**, *2005*, 3513–3523. [CrossRef]
74. Signorella, S.; Daier, V.; Ledesma, G.; Palopoli, C.; Back, D.F.; Lang, E.S.; Kopp, C.R.; Ebani, P.; Brum Pereira, M.; Giacomelli, C.; et al. Synthesis, structure and SOD activity of Mn complexes with symmetric Schiff base ligands derived from pyridoxal. *Polyhedron* **2015**, *102*, 176–184. [CrossRef]
75. Doctrow, S.R.; Huffman, K.; Marcus, C.B.; Tocco, G.; Malfroy, E.; Adinolfi, C.A.; Kruk, H.; Baker, K.; Lazarowych, N.; Mascarenhas, J.; et al. Salen-manganese complexes as catalytic scavengers of hydrogen peroxide and cytoprotective agents: Structure-activity relationship studies. *J. Med. Chem.* **2002**, *45*, 4549–4558. [CrossRef]
76. Ivanović-Burmazović, I.; van Eldik, R. Metal complex-assisted activation of small molecules. From NO to superoxide and peroxides. *Dalton Trans.* **2008**, 5259–5275. [CrossRef]
77. Liu, G.-F.; Dürr, K.; Puchta, R.; Heinemann, F.W.; van Eldik, R.; Ivanović-Burmazović, I. Chelate electronic properties control the redox behavior and superoxide reactivity of seven-coordinate manganese(II) complexes. *Dalton Trans.* **2009**, 6292–6295. [CrossRef]
78. Ramilo, C.A.; Laveque, V.; Guan, Y.; Lepock, J.R.; Tainer, J.A.; Nick, H.S.; Silverman, D.N. Interrupting the Hydrogen Bond Network at the Active Site of Human Manganese Superoxide Dismutase. *J. Biol. Chem.* **1999**, *274*, 27711–27740. [CrossRef]
79. Borgstahl, G.E.O.; Parge, H.E.; Hickey, M.J.; Beyer, W.F.; Hallewell, R.A.; Tainer, J.A. The Structure of Human Mitochondrial Manganese Superoxide Dismutase Reveals a Novel Tetrameric Interface of Two 4-Helix Bundles. *Cell* **1992**, *71*, 107–118. [CrossRef]